PONTIFICIA UNIVERSIDAD CATOLICA DE CHILE
SCHOOL OF ENGINEERING

WIRELESS SENSOR NETWORK AND SATELLITE DATA FUSION USING A DEEP LEARNING APPROACH FOR SPATIO-TEMPORAL LAND SURFACE TEMPERATURE ESTIMATION AND FORECASTING

NICOLÁS ESTEBAN CERNA ARAYA

Thesis submitted to the Office of Research and Graduate Studies
in partial fulfillment of the requirements for the degree of
Master of Science in Engineering

Advisor:
MIGUEL TORRES TORRITI

Santiago de Chile, August 2018

PONTIFICIA UNIVERSIDAD CATOLICA DE CHILE
SCHOOL OF ENGINEERING

WIRELESS SENSOR NETWORK AND SATELLITE DATA FUSION USING A DEEP LEARNING APPROACH FOR SPATIO-TEMPORAL LAND SURFACE TEMPERATURE ESTIMATION AND FORECASTING

NICOLÁS ESTEBAN CERNA ARAYA

Members of the Committee:
MIGUEL TORRES TORRITI
CHRISTIAN OBERLI GRAFF
JORGE GIRONÁS LEÓN
MARÍA JOSÉ ESCOBAR SILVA
AMADOR GUZMÁN CUEVAS

Thesis submitted to the Office of Research and Graduate Studies
in partial fulfillment of the requirements for the degree of
Master of Science in Engineering

Santiago de Chile, August 2018

ACKNOWLEDGEMENTS

This work was supported by CONICYT of Chile through CIGIDEN (Centro de Investigación para la Gestión Integrada del Riesgo de Desastres) under research grant (FONDAP 15110017) and the National Institute of Hydraulics of Chile (INH).

Contents

List of Figures

List of Tables

ABSTRACT

The estimation and monitoring of land surface temperatures (LST) over an area is relevant in the study of a diversity of environmental process because is one of the fundamental physical properties that governs the energy interaction between the Earth's surface and the atmosphere at local and global scales. Currently LST measurements over wide areas are obtained from satellites. However, remotely sensed LST does not have the temporal resolution required for adequate tracking and analysis of quick changes, whose monitoring is especially necessary in disaster management and early warning systems of hydrometeorological processes. Hence, a data fusion strategy to combine air temperature measurements from wireless sensor network (WSN) and satellite LST acquisitions is proposed for online estimation and forecasting of LST images with high temporal and spatial resolutions. The proposed approach can also be employed to reconstruct missing data or to smooth LST satellite images that may be coarse because of reprojection and resampling artifacts. The proposed spatio-temporal estimation method can provide LST estimates every 15 minutes with an average RMSE of 2.21 °C. The proposed WSN and satellite data fusion strategy can be extended to other applications and is not limited to air temperature and LST measurements. Considering that the approach can provide LST estimates between satellite passes or even when there is a cloud cover, the approach can provide a valuable tool for future environmental monitoring and hidrometeorological research.

Keywords: Land Surface Temperature (LST), Wireless Sensor Network (WSN), Deep Learning, Sensor Fusion, Real-Time.

RESUMEN

La estimación y el monitoreo de la temperatura superficial del terreno (LST, por sus siglas en inglés) sobre un área es relevante en el estudio de una diversidad de procesos ambientales debido a que es una de las propiedades físicas fundamentales que gobiernan la interacción energética entre la superficie de la Tierra y la atmósfera tanto a escalas locales como globales. Actualmente las mediciones de LST sobre grandes áreas son obtenidas por satélites. Sin embargo, la LST medida de forma remota no posee la resolución temporal requerida para un adecuado seguimiento y análisis de cambios rápidos, cuyo monitoreo es especialmente necesario en la gestión de desastres y en sistemas de alerta temprana de procesos hidrometeorológicos. Por lo tanto, se propone una estrategia de fusión de datos para combinar mediciones de temperatura del aire provenientes de redes inalambricas de sensores (WSN, por sus siglas en inglés) y mediciones satelitales de LST para realizar estimaciones en tiempo real y predicciones de imágenes de LST con una alta resolución temporal y espacial. El enfoque propuesto incluso puede ser utilizado para reconstruir datos faltantes o para suavizar imágenes de LST que puedan ser de baja resolución debido a efectos de reproyecciones y remuestreo de datos. El método propuesto para la estimación espacio-temporal puede proveer estimaciones de LST cada 15 minutos con un RMSE promedio de 2.21 °C. La estrategia propuesta para la fusión de datos entre WSN y satélites puede ser extendida a otras aplicaciones y no está limitada a la temperatura del aire y mediciones de LST. Considerando que el enfoque puede proporcionar estimaciones de LST entre pasos de satélites e incluso cuando existe cobertura de nubes, el enfoque puede probar ser una herramienta valiosa para futuras investigaciones de monitoreo ambiental e hidrometeorológico.

Palabras Claves: Temperatura Superficial del Terreno, Redes Inalámbricas de Sensores, Aprendizaje Profundo, Fusión de Sensores, Tiempo Real.

Chapter 1. INTRODUCTION

Land surface temperature (LST) is one of the fundamental physical properties that governs the energy interaction between the Earth's surface and the atmosphere at local and global scales (Li et al., 2013). Thus accurate measurement of LST is of primary importance in a variety of fields, such as biogeochemical studies, climate and environmental monitoring, ecology, hydrology, and meteorology, among other (Li et al., 2013; Buyantuyev & Wu, 2010; Wan, 2008, 1999a). However, accurately measuring LST of large regions with adequate temporal resolution is a challenge. Satellite sensors are the main source of LST data over wide areas, but with limited spatio-temporal resolutions (Khan et al., 2011; Quan et al., 2018) that are required for adequate tracking and analysis of quick changes, whose monitoring is especially necessary in disaster management and early warning systems of hydrometeorological processes (Pinto et al., 2015; Contreras Vargas et al., 2016; Martinis et al., 2013; Joyce et al., 2009).

The existing strategies to improve temporal resolution of remotely sensed variables either rely on geostationary satellites, such as GOES (Wu et al., 2015; Sun & Pinker, 2003), Feng-Yun Quan et al. (2018), or on multi-source satellite data fusion techniques (J. Zhang, 2010), typically combining Landsat and MODIS observations (Hilker et al., 2009; Shen et al., 2016; Parastatidis et al., 2017), or SAR and multispectral imagery Butenuth et al. (2011); Martinis et al. (2013). Although new geostationary satellites like GOES-16 and GOES-17 satellites can provide high temporal resolution imagery every 5 to 15 minutes, i.e. three time faster than previous probes, the estimation of LST is still limited by the coarser resolution of geostationary sensors (> 2 km in current GOES) and cloud cover (Inamdar et al., 2008; Wu et al., 2015; B. Huang et al., 2013). On the other hand, the variations of LST during the day cycle cannot be measured fast enough using multi-source satellite data fusion strategies due to the temporal resolution of the existing sensors (Zhan et al., 2013), even if recently good progress in hourly LST estimation has been achieved by Quan et al. (2018), who have developed a spatio-temporal multi-satellite data fusion model that

combines the geostationary Feng-Yu 2F, with Modis and Landsat measurements to achieve 1-hour sampling intervals, 100 m spatial resolution, and 2.5 °C RMSE errors on average.

In the above context, the main contribution of this work is the development of a method for online estimation and prediction of LST with high temporal and spatial resolutions. The novelty of the approach lies in the formulation of a data fusion strategy based on deep learning to combine satellite data with measurements obtained from a ground network of spatially distributed sensors that are wirelessly connected (wireless sensor network; WSN). The survey work of J. Zhang (2010) had pointed out that future improvements in accuracy and spatio-temporal resolution would require high-level fusion techniques combining satellite and terrestrial sensor networks, which despite the rapid technological development, remained an open challenge. Using ground-level measurements to improve estimates derived from remotely sensed data is not a new idea, but rather an essential aspect of building, calibrating and correcting models to obtain estimates of different variables of interest. Many approaches build and calibrate models off-line in different domains, from grassland and biomass measurement (Friedl et al., 1994) to improved LST estimation (Vidal, 1991). More recent works propose data fusion strategies of satellite data with ground sensors to improve time-series estimates of solar radiation (Mieslinger et al., 2014), the concentration of particulate material $PM_{2.5}$ (Lv et al., 2016), and LST (Ke et al., 2013). However, these studies have focused their efforts on the estimation of aggregated data on a daily or seasonal basis, and to the best of our knowledge, the proposed method is the first one to provide an approach for real-time satellite and WSN data fusion capable of estimating remotely sensed data from ground-level measurements, unlike the existing approaches that rely on multi-source satellite data fusion techniques (J. Zhang, 2010).

It is to be noted that the proposed approach is validated with a WSN involving only eight nodes deployed by the authors (Aldunate & Oberli, 2018; Contreras Vargas et al., 2016) in the Quebrada de Ramón watershed, which is part of the Andes mountain range in central Chile, covering an area of 4×5 km (N-S×W-E), with abrupt topography spanning

altitudes between 877 and 1751 m a.s.l. The WSN nodes correspond to 8 pixels (2% of the image) and allow to estimate the LST in the remaining area corresponding to a 25×25 km region with less than 1.4 °C error. An important advantage of using WSN measurements is that high temporal-resolution WSN data not only allows to produce LST maps with the same high temporal resolution of the WSN, but can yield measurements even during periods in which the cloud cover affects the satellite data. Thus the method can be used to reconstruct missing values in LST satellite images or to repair image artifacts produced by map reprojections. In contrast to multi-source satellite data fusion techniques, the proposed approach can be thought of as methodology to estimate remotely sensed data from ground-level measurements obtained from a WSN with very low spatial resolution but higher sampling frequency than standard satellite acquisitions.

This paper is organized as follows. The data sources and the study area are described in Section 2. The proposed approach, including the notation and preliminary definitions are explained in Section 3. The performance results of the approach, as well as that of its spatial and temporal components, are presented in Section 4, followed by final concluding remarks in Section 5.

Chapter 2. DATA SOURCES AND STUDY AREA

The proposed method for generating high temporal resolution LST images uses two sources of data: air temperature measurements from a WSN, and historical data of LST satellite images. The WSN comprises eight nodes with a temporal resolution of 15 minute located at the Quebrada de Ramón basin ($33^\circ\ 26'\ 29''$ S, $70^\circ\ 27'\ 36''$ W) on the east of Santiago city over the foothills of the Andes mountain range, as illustrated in Fig. 2.1a. Each temperature sensor is implemented using an integrated circuit sensor SHT21 by Sensirion AG, with a measurement accuracy of ± 0.3 °K. As for the remotely sensed data, we employed imagery produced by NASA's MODIS satellites TERRA and AQUA. The accuracy of the current MODIS LST measurements is within 0.5 °K, (Wan, 2014); see (Wan, 1999b) for further details on the theoretical basis for LST computation. Specifically, LST products MOD11 and MYD11 Level-2 were selected because of their spatial resolution (1 km) and high availability about every six hours per day of the combined TERRA and AQUA products. The MOD11 A MODIS LST image of the study area showing the 1 km pixels is presented in Fig. 2.1b

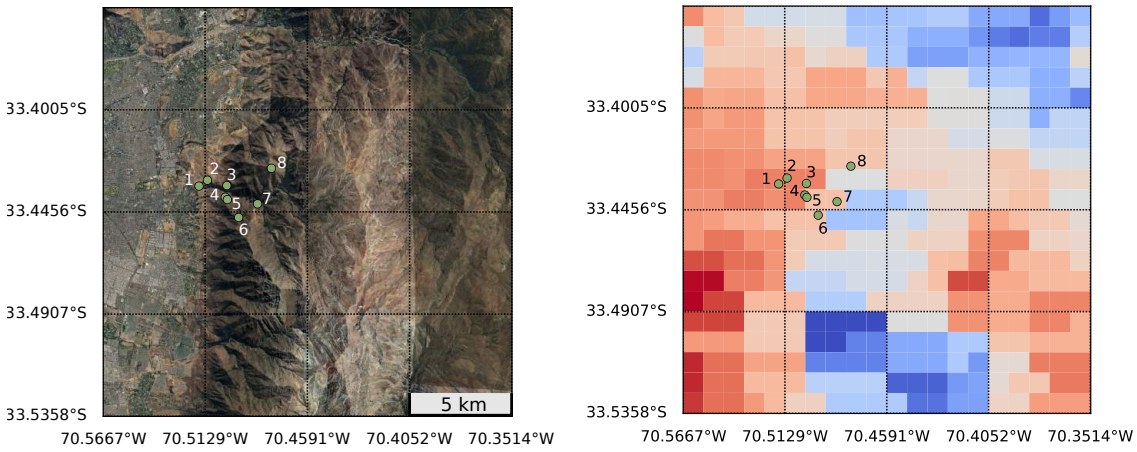

(A) (B)

FIGURE 2.1. Distribution of WSN nodes in the study area: (a) satellite view, (b) view on MODIS LST MOD11/MYD11 Level-2 image.

Wireless sensor network data was collected from August 2016 to June 2018, taking samples every 10 minutes, representing 64,224 air temperature measurements for each one

of the nodes. The location, altitude and positions of each sensor of the network are presented in Table 2.1.

TABLE 2.1. WSN sensor node locations.

Sensor ID	**Latitude**	**Longitude**	**Altitude (m a.s.l.)**	**Corresponding Position in the LST Image**
1	-33.434	-70.516	877.8	(8,4)
2	-33.431	-70.511	947.7	(8,5)
3	-33.433	-70.501	999.6	(8,6)
4	-33.439	-70.502	1166.7	(9,5)
5	-33.440	-70.501	1236.3	(9,6)
6	-33.448	-70.495	1471.7	(10,6)
7	-33.434	-70.485	1338.1	(9,7)
8	-33.426	-70.478	1751.4	(7,8)

Remotely sensed data was acquired from 24 February 2000 to 26 June 2018, amounting to 27,198 land surface temperature images. Only very few images with no available data for any of the pixels within the study area were removed from the data set. The histograms of LST images along years and day times are shown in Fig. 2.2. It is possible to observe in Fig. 2.2a that the production of MODIS MOD11 and MYD11 LST images covering the study area has been practically constant since 2004, with roughly 1600 images per year. The times of the day at which most of the images were acquired by the satellites are 3 AM, 6 AM, 3 PM and 6 PM, as shown in Fig. 2.2b.

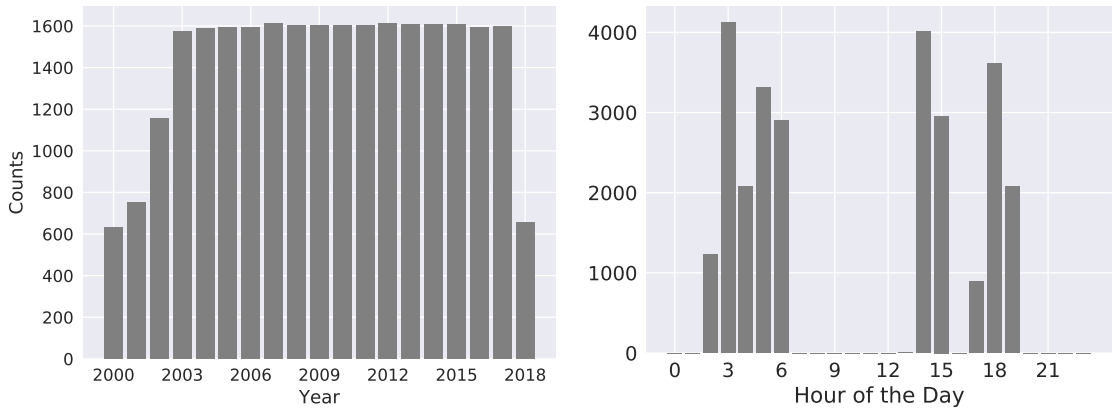

(A) (B)

FIGURE 2.2. Histograms of LST data showing the distribution of acquisitions by year and hour of the day.

Chapter 3. PROPOSED APPROACH

This section explains the proposed method, starting with the basic notation and definitions that will be useful for a clear exposition of the approach and its different stages.

3.1. Notation and Preliminary Definitions

In order to explain the proposed data fusion approach, it will be useful to firstly explain the notation adopted to represent measurements from the distinct data sources with different spatio-temporal resolutions.

3.1.1. Wireless Sensor Network Data

Data from a WSN can be represented as a matrix $\boldsymbol{W}_{M\times N}$, where M is the number of sampling instants (measurements) and N is the number of sensor nodes in the network. An element $w_{i,j} \in \boldsymbol{W}_{M\times N}$ corresponds to the i-th sample acquired by the j-th sensor node in the network. Missing elements for which it was not possible to obtain a measurement sample $w_{i,j}$ will be denoted by $\varnothing$. A set of samples from all N sensor nodes of the network at instant i is denoted by $\boldsymbol{w}_{i,*}$. These acquisition times are stored in a vector $\boldsymbol{t}$ whose components are denoted by t_i. The difference between two consecutive components of $\boldsymbol{t}$ is fixed and equal to the sampling period of the network, T_w, i.e. $t_{i+1} - t_i = T_w,\ i = 0, 1, \ldots, M$. Estimated measurements at time t_i will be indicated by $\hat{\boldsymbol{w}}_{t_i,*}$, while predicted measurements k sampling intervals ahead at time $t_{i+k} = t_i + kT_w$ using information until time t_i will be denoted by $\hat{\boldsymbol{w}}_{t_{i+k}|t_i,*}$. Missing network measurement samples $\varnothing$ at sampling instant i will be replaced by imputed values denoted by $\bar{\boldsymbol{w}}_{i,*}$ through an imputation process explained in the following section. It is to be noted that sampling instants t_i cannot be replaced simply by index i because satellite measurements take place at different chronological time instants and distinct non-uniform sampling intervals. Therefore, this way of indexing the WSN estimations and forecasts is necessary to avoid confusion.

3.1.2. Satellite Imagery Data

Satellite LST data can be represented as a multidimensional matrix $\boldsymbol{S}_{P\times R\times C}$, i.e. a stack of P matrices with R rows and C columns. Here P corresponds to the total number of satellite acquisitions or passes. The p-th matrix (LST image or map) in the stack is denoted by $\boldsymbol{S}_{p,*,*}$, and an the value of an element of that image $\boldsymbol{S}_{p,*,*}$ in row u and column v is denoted by $s_{p,u,v}$, or for brevity as $s_{p,\boldsymbol{r}_j}$, when $\boldsymbol{r}_j = (u_j, v_j)$ corresponds to the pixel in which the j-th sensor node of the WSN is located. Each satellite acquisition $p \in [1, 2, \ldots, P]$ can be associated with a sampling instant τ_p, stored in a vector $\boldsymbol{\tau}$. Estimated images at time $t_i \in \boldsymbol{t}$ will be denoted by $\hat{\boldsymbol{S}}_{t_i,*,*}$, while predicted images k sampling intervals ahead for sampling intervals $T = T_w$ using information up to time t_i, i.e. predicted at time $t' = t_i + kT = t + kT_w$, will be denoted by $\hat{\boldsymbol{S}}_{t_{i+k}|t_i,*,*}$. The image with acquisition time τ closest to WSN time t_i will be denoted by $\boldsymbol{S}_{t_i,*,*} = \boldsymbol{S}_{p,*,*}$, with $p = \operatorname{argmin}_{p\in\{1,2,\ldots,P\},\tau_p\in\boldsymbol{\tau}} \|t_i - \tau_p\|$. It is to be noted that $\boldsymbol{S}_{t_i,*,*}$ is not an acquisition at time t_i, but simply an image $\boldsymbol{S}_{t_i,*,*} \in \boldsymbol{S}_{P\times R\times C}$ and should not be confused with estimated images at time t_i denoted by $\hat{\boldsymbol{S}}_{t_i,*,*}$. Considering the previous definitions, it should be observed that estimated or predicted LST maps can be computed at rate equivalent to the sampling period T_w of the WSN.

3.2. Proposed Method

A process with different stages that model the temporal evolution of the air temperature measurements in $\boldsymbol{W}_{M\times N}$ acquired by the WSN and their relation to satellite LST measurements in $\boldsymbol{S}_{P\times R\times C}$ is developed using deep neural networks (DNN) to estimate LST images $\hat{\boldsymbol{S}}_{t_{i+k}|t_i,*,*}$ at t_i. All estimation stages employ fully connected multi-layer perceptron DNNs (Goodfellow et al., 2016), except for process that performs the temporal forecasting of air temperatures, which a recurrent neural network (RNN). RNN are DNN that have connections that form a directed graph over the elements of a sequence, thus can capture the dynamic temporal behavior of time sequences. More specifically, the underlying units of the implemented RNN are long short-term memory (LSTM) networks, which are well

known for their ability to classify and make predictions based on time series data (Goodfellow et al., 2016).

The proposed method involves three main stages, which are shown in the block diagram of Fig. 3.1. First, the WSN measurements $\boldsymbol{w}_{i,*}$ at time t_i are passed to the imputer responsible for replacing possible missing data $\varnothing$ by estimates $\bar{\boldsymbol{w}}_{i,*}$. The second stage generates predictions $\bar{\boldsymbol{w}}_{t_{i+k},*}$ of future WSN measurements k sampling periods ahead. The forecasted values are employed in the last stage to produce LST estimates $\hat{\boldsymbol{S}}_{t_i,*,*}$ and forecasts $\hat{\boldsymbol{S}}_{t_{i+k},*,*}$, at instants $k = 1, 2, \ldots,$. The proposed strategy relies on the fact that the temporal resolution of the WSN is much higher than the one of the satellites. Hence, when a satellite image is received, it is always possible to match the acquisition with a measurement from the WSN. On the other hand, satellite derived LST measurements and air temperatures measured by the WSN sensor nodes are correlated and exhibit continuity properties. The average rate of change of WSN air temperature measurements in the study area is 0.015 $^{\circ}\mathrm{C}/min$, which is relatively slow. On the other hand, the sampling period of the WSN ensures the data is acquired frequently enough, well above the Nyquist frequency required to reconstruct LST considering the daily/yearly cycle of LST temperatures. In fact, the frequency spectrum of the temperature data shows that the Nyquist frequency would be around $6 \cdot 10^{-4}$ Hz, while the WSN sampling frequency is $1/600$ Hz $\approx 1.67 \cdot 10^{-3}$ Hz, which is about 3 times the Nyquist frequency.

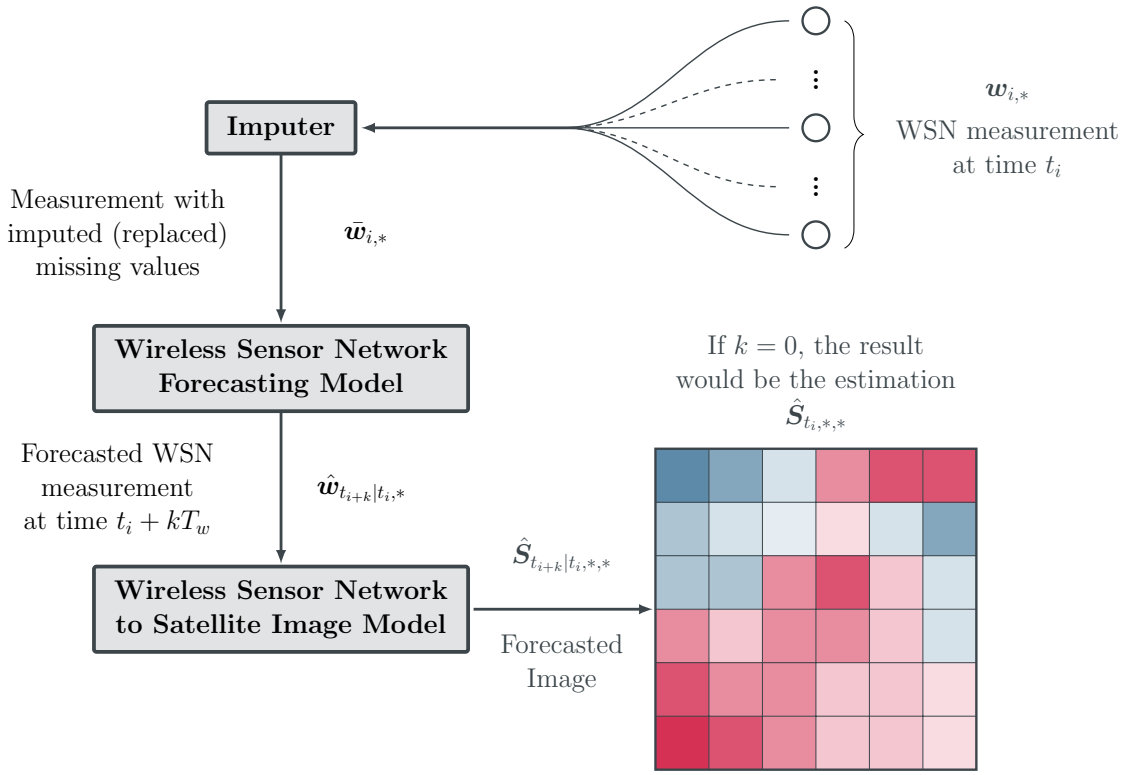

FIGURE 3.1. Main stages of the proposed method: imputation, WSN forecasting, LST estimation and forecasting.

A spatio-temporal representation of the WSN and satellite data fusion process for LST estimation and forecasting is presented in Fig. 3.2. The air temperature measurements $w_{i,j}$, $= 1, 2, 3, \ldots, N$ are shown in the bottom level of Fig. 3.2. The measurement $w_{i,2}$ if the second sensor node is missing, thus is connected by a dotted line to the second level, which represents the imputation stage that will replace $w_{i,2} = \varnothing$ by $\bar{w}_{i,2}$. The third level carries out the computation of temperature forecasts $\bar{w}_{t_{i+k}|t_i,j}$, $j = 1, 2, \ldots, N$ for the N nodes in the WSN network using a LSTM-RNN (Goodfellow et al., 2016). In the fourth level, the forecasted air temperatures $\bar{w}_{t_{i+k}|t_i,j}$, $j = 1, 2, \ldots, N$ are converted to LST estimates at the locations of the sensor nodes using air-to-land surface temperature model $f_j : \bar{w}_{t_{i+k}|t_i,j} \rightarrow \bar{s}_{t_{i+k}|t_i,\boldsymbol{r}_j}$ that yields LST estimates $\bar{s}_{t_{i+k}|t_i,\boldsymbol{r}_j}$ at the location of each of the sensor nodes $j = 1, 2, \ldots, N$. It is to be noted that a model f_j based on multilayer perceptrons is learnt for each sensor node location from historical LST data in $\boldsymbol{S}_{P\times R\times C}$ and the WSN

data in $\boldsymbol{W}_{M\times N}$. Finally, another spatial estimation model, also implemented using DNNs of multilayer perceptrons generates LST estimates $\hat{\boldsymbol{S}}_{t_i,*,*}$ and forecasts $\hat{\boldsymbol{S}}_{t_{i+k},*,*}$, at instants $k = 1, 2, \ldots,$. The following subsections explain each individual stage in more detail.

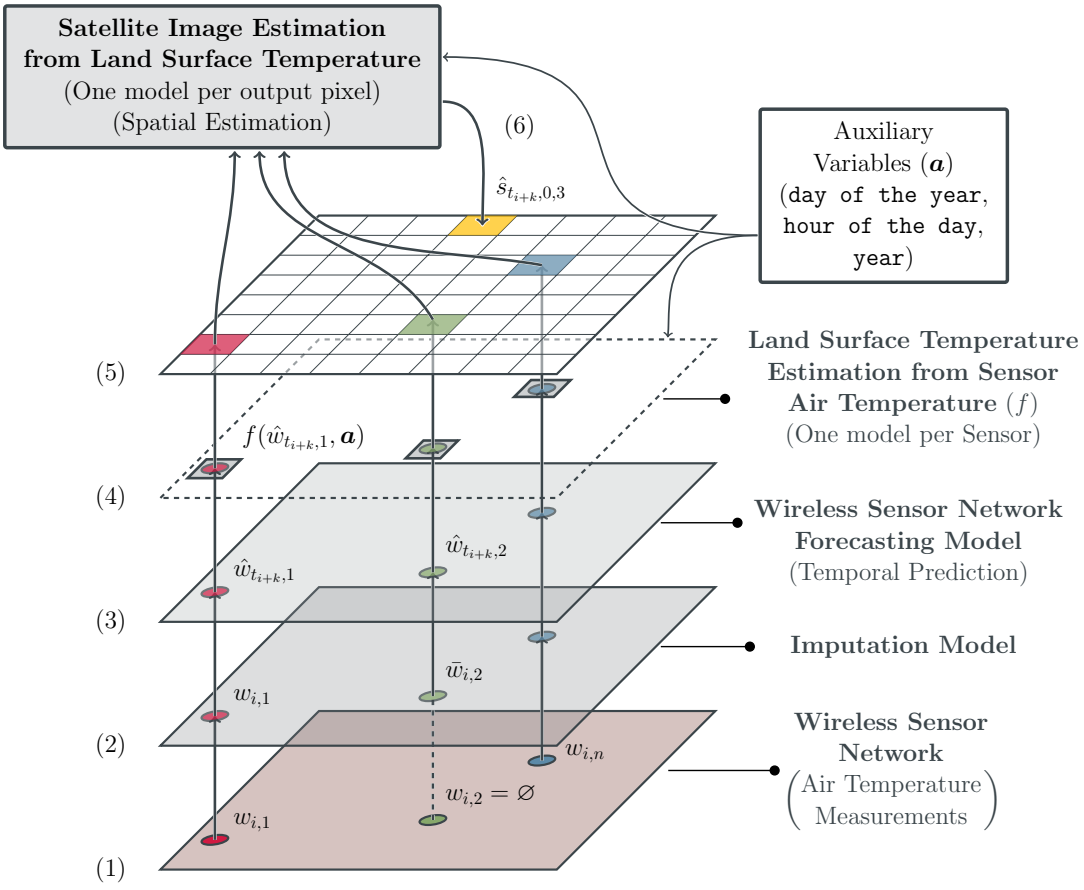

FIGURE 3.2. Spatio-temporal representation of the WSN and satellite data fusion process for LST estimation and forecasting.

3.2.1. Imputation Process

Missing data due to errors in data acquisition is a common problem in environmental research. These gaps of information are an important obstacle for the prediction of time-series because normally prediction processes require data to be continuously fed without interruptions (Junninen et al., 2004). Usual methods for imputing missing data are based on simple algorithms, such as mean substitution, interpolation, smoothing, and curve fitting, or statistical methods based on regression analysis, or autoregressive models. However, the

former are not suited for inferring variables with high time dependence and a strong seasonality like temperature. On the other hand, standard time series analysis and autoregressive models yield unsatisfactory results with datasets that present large periods of missing data. Therefore, the proposed imputation process to replace possible missing values $w_{i,j} = \varnothing$ at sampling instant i of one or more sensor nodes $j = 1, 2, \ldots, N$, by estimates $\bar{w}_{i,j}$ relies on the close relationship between measurements of the network's sensors and the fact that is very unlikely to have intermittence in many sensors simultaneously. To this end, a multilayer perceptron DNN is implemented to capture the relationship between the sensor nodes of the WSN and produce sensor outputs for the missing ones from the available ones. One novel aspect of the implemented neural network is that the model takes into account information about sensor failures to adjust the imputation process accordingly. The information about sensor failure is used as an input of the neural network as will be explained next.

The percentage of missing values for each one of the sensors nodes in the WSN dataset computed over a total of $M = 64,224$ measurement instants are shown in Fig. 3.3a. On the other hand, the histogram of simultaneously missing values in a measurement ($w_{i,*}$) shown in Fig. 3.3b confirms that there are always at least two operational sensor nodes, or three operational nodes 99.95% of the time considering the total number of nodes is $N = 8$. Only less than 3% of the measurements have 2 missing values at the same time and less than 1.5% of the measurements have three missing values simultaneously. It is also to be noted that each sensor node of the WSN has a different probability of including missing data as can be seen in Fig. 3.3a. Assuming failures of sensor nodes in the WSN are statistically independent, the event of having missing values in the measurement of j-th node of the WSN can be modeled as a Bernoulli-distributed random variable $X_j \sim B(1, p_j)$, where p_j is the probability of finding a missing value in the j-th component of the measurement vector $w_{i,*}$ at any time instant i. The probability p_j of having missing values in node $j = 1, 2, \ldots, N$ is computed from the data in $\boldsymbol{W}_{M \times N}$ and summarized in Table 3.1.

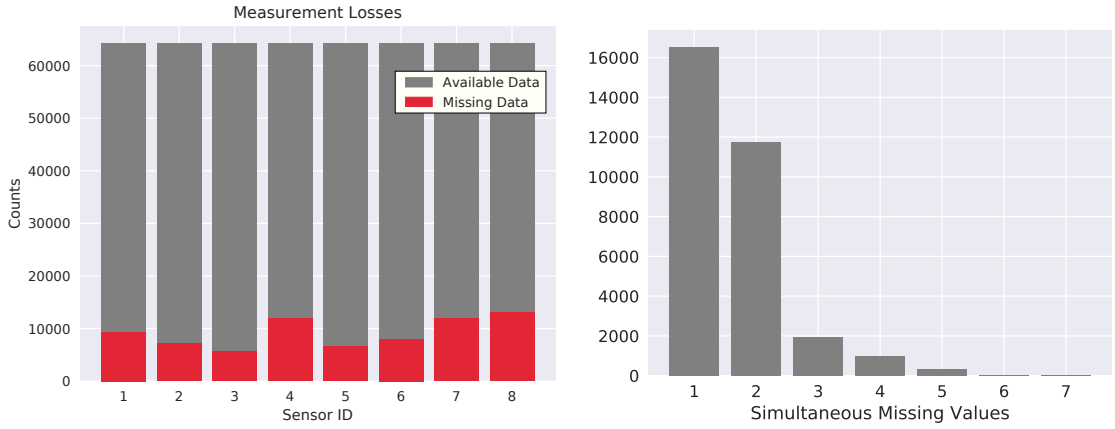

(A) (B)

FIGURE 3.3. Missing values in the wireless sensor network measurements.

TABLE 3.1. Probabilities p_j of finding a missing value for each sensor node of the WSN.

1	**2**	**3**	**4**	**5**	**6**	**7**	**8**
0.1457	0.1109	0.0884	0.1863	0.1036	0.1245	0.1846	0.2033

A training dataset $\boldsymbol{W}_T$ composed of 49,727 measurements in $\boldsymbol{W}_{M\times N}$ was employed to build the DNN model. The first step of the training process involved the removal of measurement vectors with empty data from the training dataset, leaving only a subset of 23,784 complete measurements per sensor. Then 23,784 realizations taking values 0 or 1 were drawn from Bernoulli distributions $Y_j \sim B(1, 1-p_j)$ with $j = 1, 2, \ldots, 8$. The process Y_j simulates good sensor measurements that do not have missing values. The realizations of Y_j for each of the nodes was stored in an auxiliary matrix $\boldsymbol{A}$ with the same size to that of the training dataset, as shown in Fig. 3.4. After building matrix $\boldsymbol{A}$, a new matrix $\boldsymbol{B} = (\boldsymbol{W}_T \circ \boldsymbol{A} + \neg\boldsymbol{A} \cdot \varnothing)$ was constructed, where $\circ$ is the Hadamard product, was constructed to simulate missing values with a sensor failure rate equivalent to that of the WSN. The empty values were treated as hyperparameters of the training process, which were replaced by a constant value corresponding to the mean temperature registered by the sensor node. The inputs to the DNN during the training process were the rows of $\boldsymbol{A}$ and

$\boldsymbol{B}$, while the outputs were the values of $\boldsymbol{w}_{i,*}$. It should be noted that the rows of $\boldsymbol{A}$ act as auxiliary vectors that encode the presence or absence of data in a component of $\boldsymbol{w}_{i,*}$ as shown by the inputs to the neural network illustrated in Fig. 3.5. The main parameters of the neural network implemented for the imputation process are shown in Table 3.2. The idea behind the proposed learning strategy to build the imputation model is that by telling the neural network which sensors have good data, it can focus the learning effort on the useful input data, this in turn allows the neural network to learn better the stochastic behavior of the WSN node failures and how to handle missing measurements at any given instant.

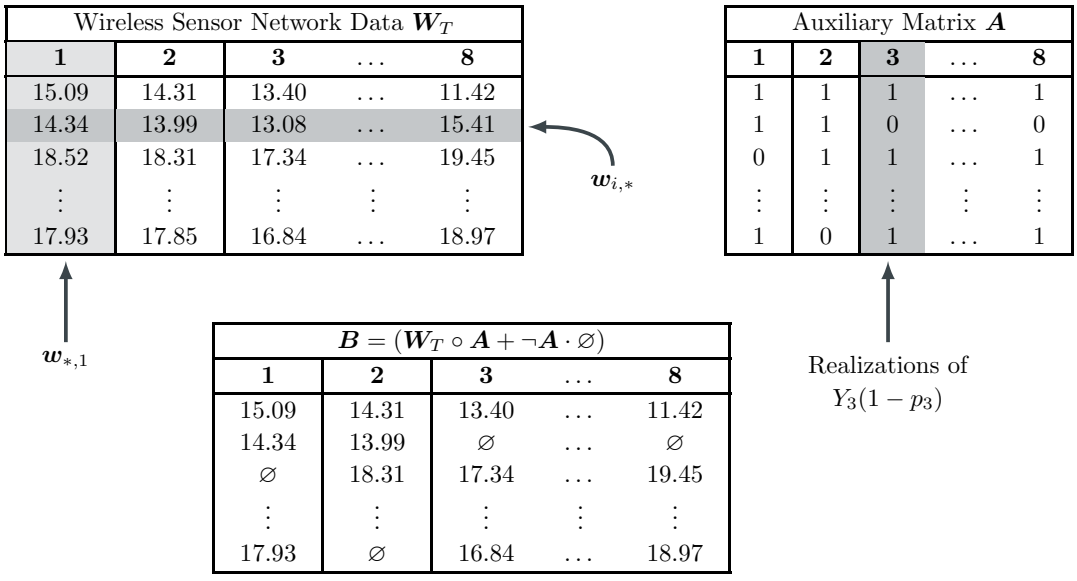

FIGURE 3.4. Preprocessing of the training dataset for the imputation model.

TABLE 3.2. Main parameters of the DNN implemented for the imputation process.

Optimizer	Error	Activations	Layers Size
LM-BFGS	RMS	TANH	Input: 16 Hidden: (200, 200) Output: 8

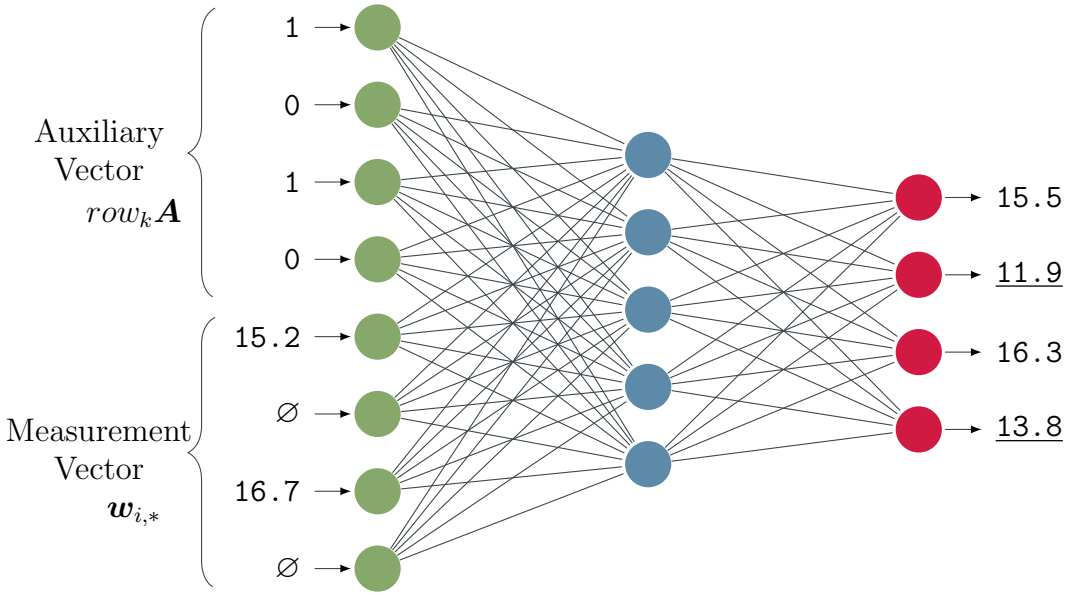

FIGURE 3.5. Graphical representation of the neural network for the imputation process. The true sizes of each layer and number of hidden layers are shown in Table 3.2.

The testing procedure for the proposed imputation model was identical to the one described for the training process, with the difference that the outputs of the neural network were compared to the actual values in order to calculate the reconstruction errors. The error calculation employs only the outputs corresponding to the missing values and not the whole reconstructed vector of measurements $\bar{\boldsymbol{w}}_{i,*}$. The root-mean squared error (RMSE) of the imputed values $\bar{\boldsymbol{w}}_{i,*}$ compared to the ground truth are summarized in Table 3.3, which shows an average temperature RMSE of 0.65 °C when there is only one missing value, and 0.77 °C where there are four missing values. The results of the imputation process applied to some sequences with missing measurements can be visualized in Fig. 3.6 as highlighted (darker) dots.

TABLE 3.3. RMSE for the reconstruction made by the imputation process. The last column shows the error and standard deviation for any number of missing inputs.

Number of sensors failing simultaneously	**1**	**2**	**3**	**4**	**1 to 7 (Operational)**
RMSE (°C)	0.606	0.673	0.711	0.766	0.648
Std. Dev. (°C)	0.031	0.023	0.062	0.307	0.015

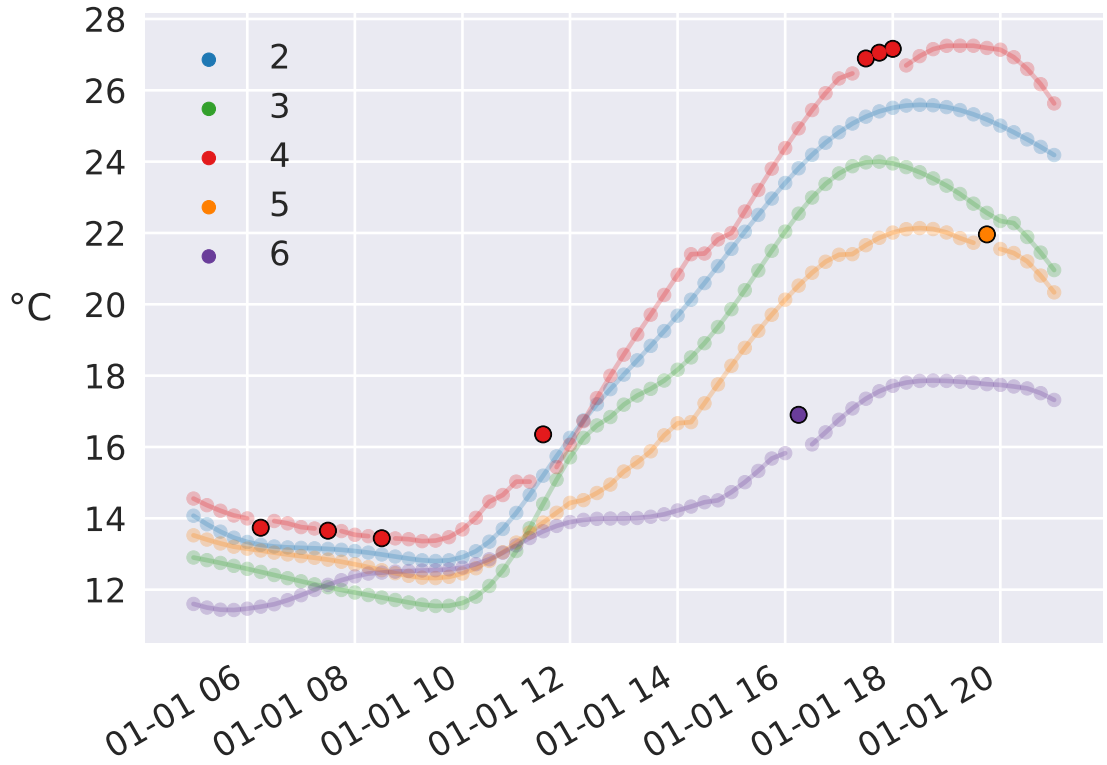

FIGURE 3.6. Example of missing values computed by the imputer process using the remaining sensors, using original missing data.

3.2.2. Wireless Sensor Network: Forecasting Model

The model to forecast air temperature measurements $\hat{\boldsymbol{w}}_{t_{i+k}|t_i,*}$ using the WSN temperature estimates $\hat{\boldsymbol{w}}_{t_i,*}$ is implemented using a recurrent neural network (RNN) with LSTM (Long Short-Term Memory) units because of its greater ability to describe the temporal

dynamics of time series as previously mentioned. The purpose of this model is to predict future values of the WSN air temperature measurements at the sensor node locations that will be used in the following stage to produce the LST estimates $\hat{\boldsymbol{S}}_{t_i,*,*}$ and forecasts $\hat{\boldsymbol{S}}_{t_{i+k},*,*}$, at instants $k = 1, 2, \ldots,$.

A graphical representation of the LSTM-RNN employed for air temperature forecasting is presented in Fig. 3.7. The main parameters of the LSTM-RNN are summarized in Table 3.4. The number of measurement time instants is $m = 12$ and the forecasting horizon is $k = 5$ time intervals. It is to be noted (see Fig. 3.7) that air temperature acquisition time and day of the year are used as inputs represented by a 4-component vector that encodes the daily and yearly cyclic behavior. More specifically, given a cyclic variable f_0 with values in an interval $[a, b)$, a representation that encodes the periodic behavior of f_0 over intervals $[a, b)$ is given by a tuple (f_1, f_2), where:

$$\begin{aligned} f_1 &= \cos\left(\frac{2\pi f_0}{b-a}\right), \\ f_2 &= \sin\left(\frac{2\pi f_0}{b-a}\right). \end{aligned} \tag{3.1}$$

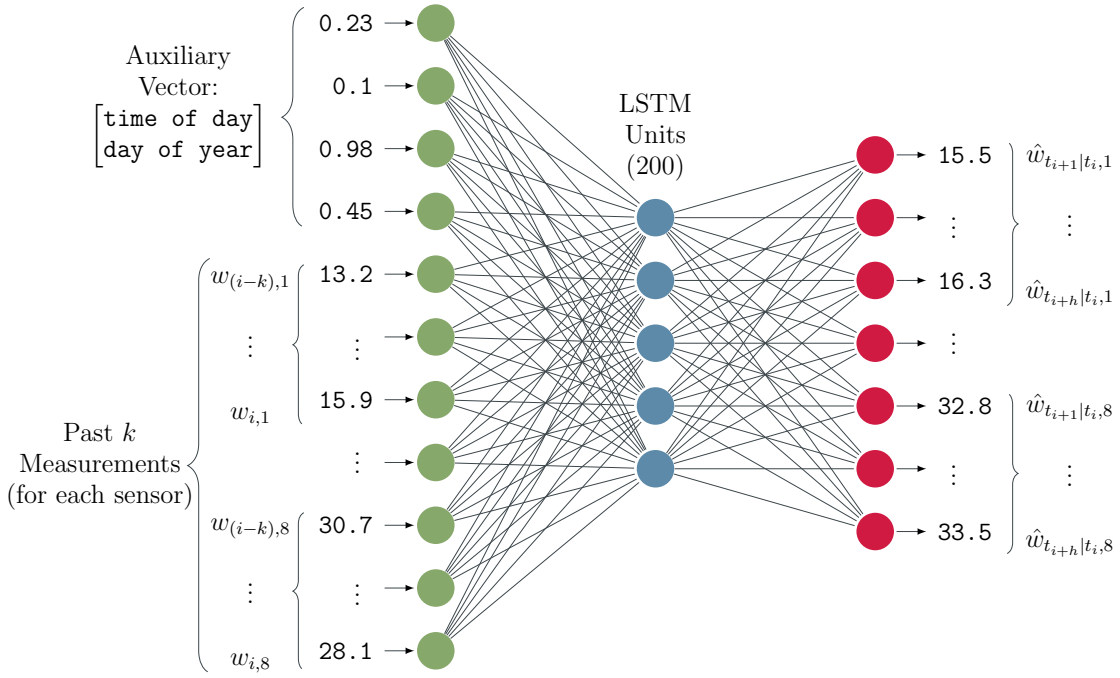

FIGURE 3.7. Graphical representation of the LSTM-RNN for the forecasting model. The true sizes of each layer and number of hidden layers are shown in Table 3.4.

TABLE 3.4. Main parameters of the LSTM-RNN for WSN air temperature forecasting. LSTM unit parameters are highlighted in bold fonts.

Optimizer	**Error**	**Activations**	**Layers Size**
ADAM	RMS	Hyperbolic tangent (Regular) **Hard sigmoid** (Recurrent)	Input: 10 Hidden: (**200**) Output: 96

The LSTM-RNN was trained with WSN data from January 1 to April 13, 2018, amounting to 9,792 measurements per sensor. WSN measurements from April 14 to May 31, 2018, corresponding to 4,687 measurements per sensor, were employed for testing. Missing values were filled by the imputer proposed in Section 3.2.1. The LSTM-RNN was trained to predict the measurements of each sensor at multiple time steps in the future using six previous consecutive measurements and their corresponding acquisition times as input. Each

output comprehends between one to twelve time steps in the future with each time-step corresponding to 15 minutes. The forecast errors for future sampling instants $k = 1, 2, \ldots, 12$ are shown in Table 3.5. A comparison of the ground truth and the forecasted air temperature values one sampling instant ahead ($k = 1$) and twelve sampling instants ahead ($k = 12$) are shown in Fig. 3.8 and 3.9, respectively.

TABLE 3.5. RMSE of the forecasted air temperatures $\hat{\boldsymbol{w}}_{t_{i+k}|t_i,*}$ [°C] for the locations of the WSN sensor nodes at different time steps $k = 1, 2, \ldots, 12$.

1	**2**	**3**	**4**	**5**	**6**
0.682	0.704	0.767	0.858	0.961	1.066
7	**8**	**9**	**10**	**11**	**12**
1.166	1.255	1.331	1.405	1.469	1.534

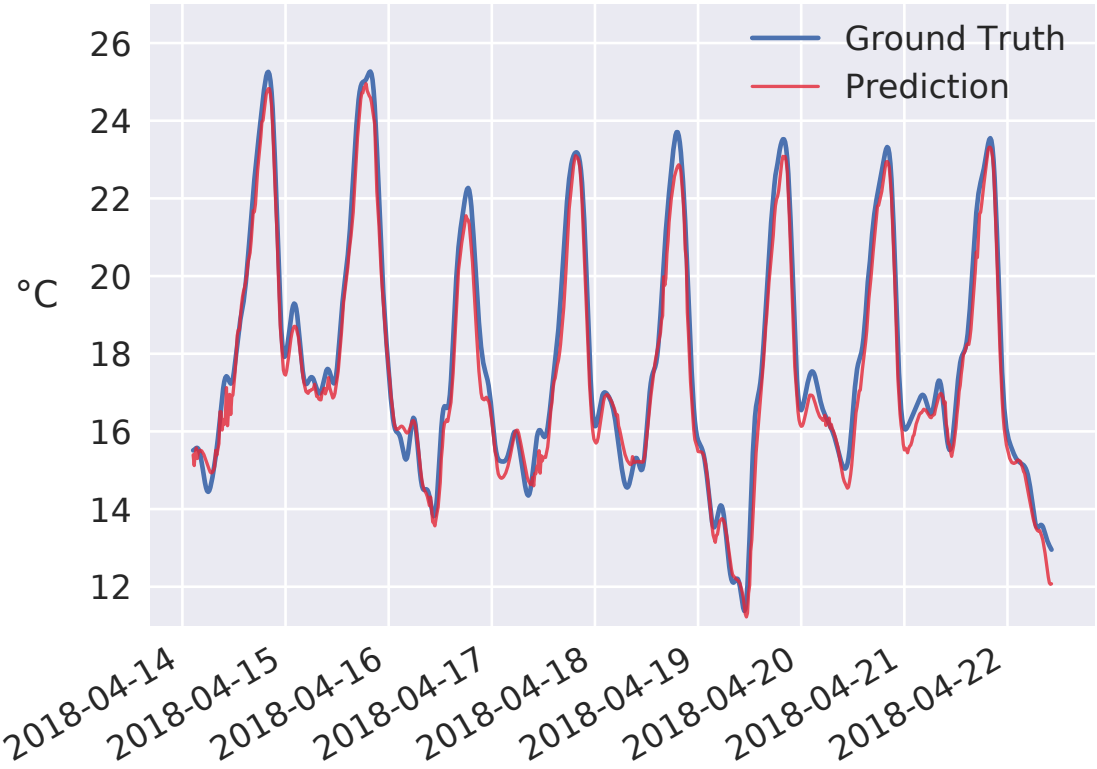

FIGURE 3.8. One step forecast (15 min.) for sensor $j = 3$ during an eight day period.

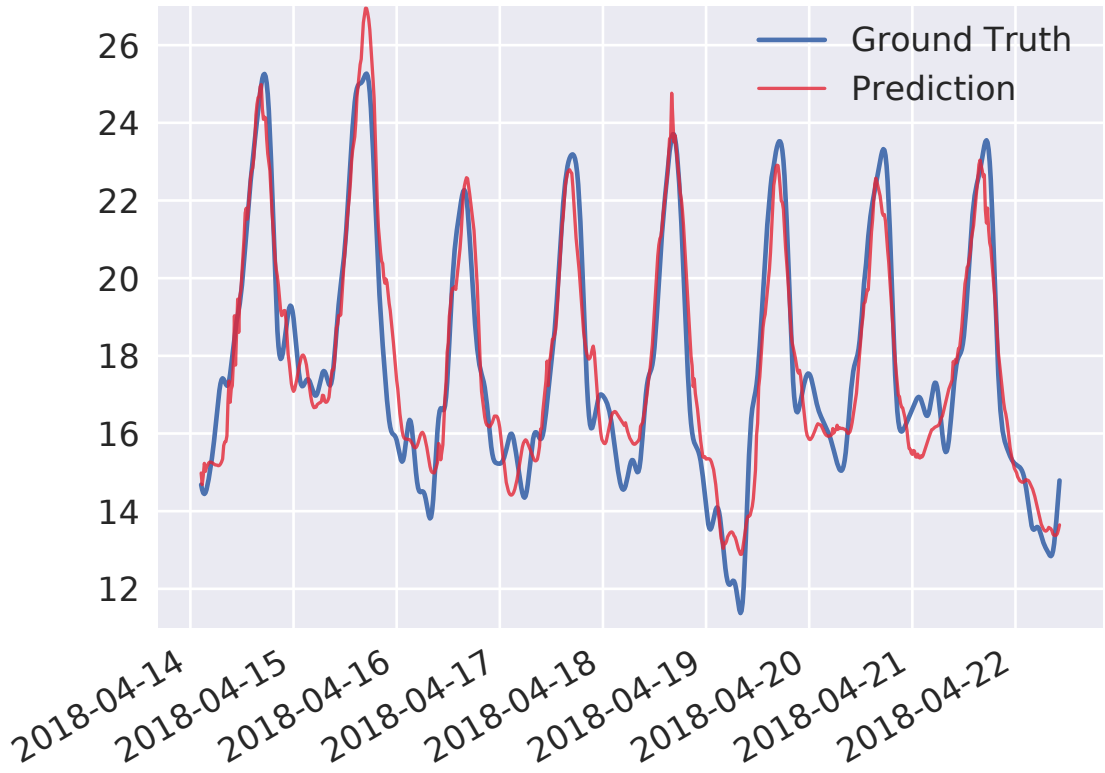

FIGURE 3.9. Twelve step forecast (3 hrs.) for sensor $j = 3$ during an eight day period.

3.2.3. Land Surface Temperature Estimation From Air Temperature Sensors

Some studies have used land surface temperature to obtain extrema or mean air temperature (L.-w. Zhang et al., 2013; Benali et al., 2012; Vancutsem et al., 2010; R. Huang et al., 2015; Kloog et al., 2014). To the best of our knowledge there is no published work to date that has tried the opposite, i.e. obtaining land surface temperature from air temperature measurements, or to compute the instantaneous relationship between these two variables. However, the correlation between land surface temperature, in particular the MODIS derived LST and air temperature has been shown in (Mutiibwa et al., 2015) to be strong, suggesting that it would be possible to obtain a model to infer LST from air temperature measurements. Thus here a set of Air to Land Surface Temperature models $f_j : \bar{w}_{t_{i+k}|t_i,j} \rightarrow \bar{s}_{t_{i+k}|t_i,\boldsymbol{r}_j}$, $j = 1, 2, \ldots, N$, that yields LST estimates $\bar{s}_{t_{i+k}|t_i,\boldsymbol{r}_j}$ at the location $\boldsymbol{r}_j$ of each of the sensor nodes $j = 1, 2, \ldots, N$ from forecasted air temperatures $\bar{w}_{t_{i+k}|t_i,j}$ is developed using DNNs of multilayer perceptrons.

A graphical representation of the DNN that implements the model $f_j : \bar{w}_{t_{i+k}|t_i,j} \rightarrow \bar{s}_{t_{i+k}|t_i,\boldsymbol{r}_j}$ is shown in Fig. 3.10. The main parameters of the DNN model are summarized in Table 3.6. The inputs to each network are the air temperature measured by the sensor $\bar{w}_{t_{i+k}|t_i,j}$, the time of the day and the day of the year, both encoded using Eq. (3.1), as in the case of the temperature forecasting model explained in the previous section. Including the time of the day and day of the year allows the DNN to learn the cyclical nature of daily temperatures and their seasonality along the year, greatly improving the accuracy of the DNNs' output. However, unlike the DNN model for air temperature estimation and forecasting, the DNNs that estimate the LST $\bar{s}_{t_{i+k}|t_i,\boldsymbol{r}_j}$ use only the air temperature value $\bar{w}_{t_{i+k}|t_i,j}$ corresponding to the sensor node j and not the set $\bar{\boldsymbol{w}}_{t_{i+k}|t_i,j}$ of all air temperature values of the WSN. It was observed that taking the measurements from other sensors as input to model the LST in the position of a given sensor node was detrimental to the performance of the neural network. The results obtained in the design phase also showed that shallow networks with just one hidden layer worked better for the purpose of estimating LST from air temperature measurements at the location of each sensor node.

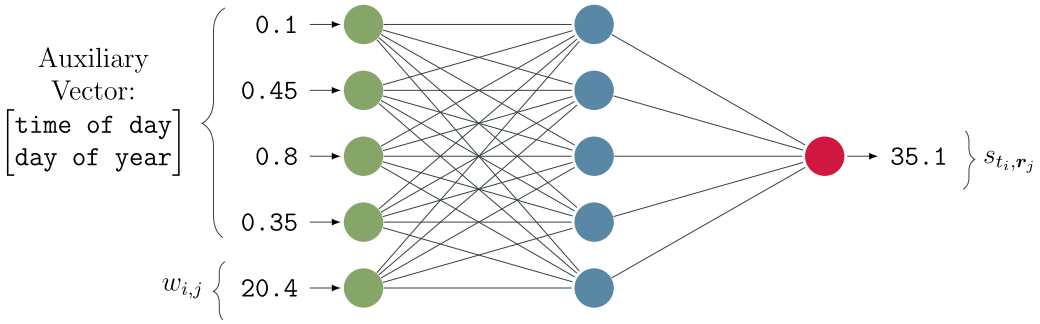

FIGURE 3.10. Graphical representation of the neural network model implemented to estimate LST from air temperature measurements at the location $\boldsymbol{r}_j$ of each WSN sensor node. The true sizes of each layer and number of hidden layers are shown in Table 3.6.

TABLE 3.6. Main parameters of the DNN models implemented to estimate LST from air temperature measurements at the location of each WSN sensor node.

Optimizer	**Error**	**Activations**	**Layers Size**
LM-BFGS	RMS	ReLU	Input: 5 Hidden: 100 Output: 1

The training process employed 600 samples amounting to 66% of the WSN and MODIS data collected before 2018, the remaining data was employed for testing (300 samples). The LST estimation RMSE values are summarized in Table 3.7 for each air-to-LST model associated to each node in the WSN. An example of the good match between LST values estimated from air temperature measurements obtained from the sensing node $j = 6$ using the neural network model built are presented in Fig. 3.11.

TABLE 3.7. RMSE values for LST estimated from air temperature measurements at each sensor node using the *Air to Land Surface Temperature* models.

Air to Land Surface Temperature

RMS Errors per Sensor Model (°C)

1	**2**	**3**	**4**	**5**	**6**	**7**	**8**
2.009	2.091	2.359	1.904	2.364	2.121	2.494	2.003

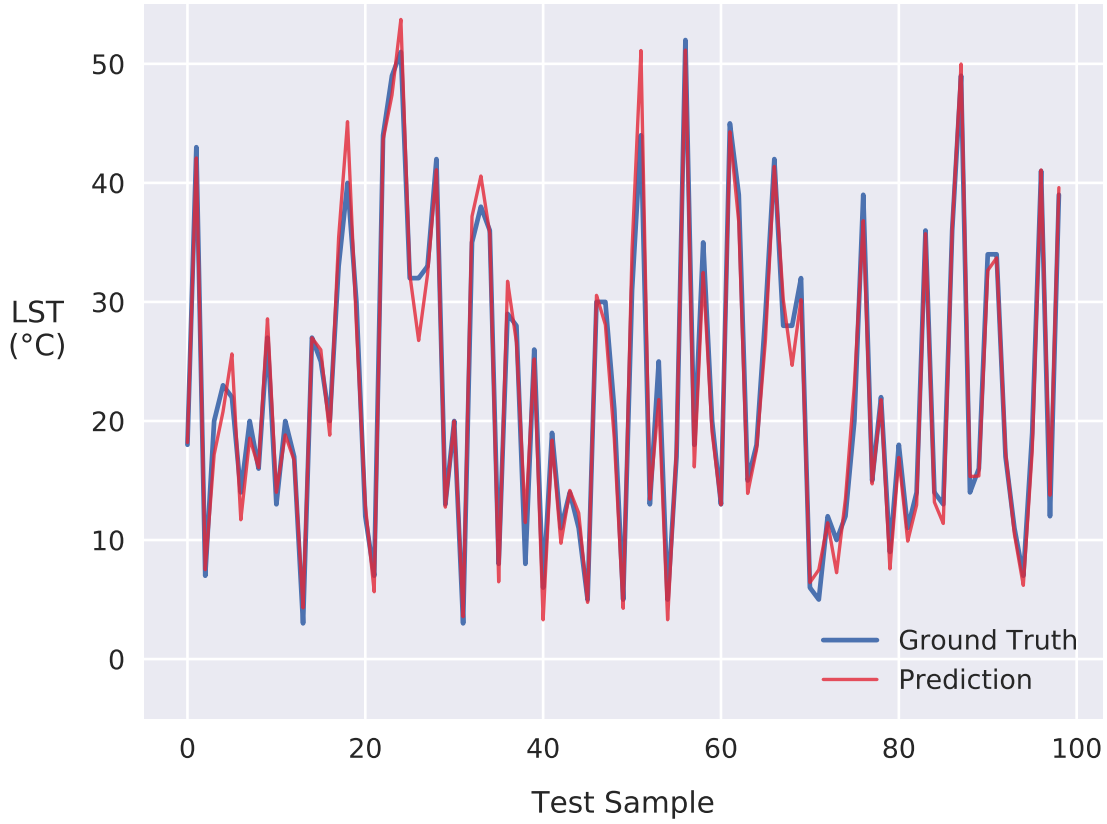

FIGURE 3.11. LST estimation from 100 samples of air temperature measurements in the evaluation set of sensor node $j = 6$.

3.2.4. Spatial Estimation of LST from WSN Measurements

This last process implements a spatial estimation model using DNNs of multilayer perceptrons to generate LST estimates $\hat{\boldsymbol{S}}_{t_i,*,*}$ and forecasts $\hat{\boldsymbol{S}}_{t_{i+k},*,*}$, at instants $k = 1, 2, \ldots,$ for the area of interest from the set $\boldsymbol{s}_{t_i,*} = \{s_{t_i,\boldsymbol{r}_1}, s_{t_i,\boldsymbol{r}_1}, \ldots, s_{t_i,\boldsymbol{r}_N}\}$ of LST values at each sensor node location as illustrated in Fig. 3.12. A graphical representation of the DNN implemented for the spatial LST estimation is shown in Fig. 3.13. The main parameters of the spatial LST estimation model are summarized in Table 3.8. A neural network for each pixel location of the satellite image was trained. The inputs to each model are the set $\boldsymbol{s}_{t_i,*}$ of land surface temperatures at the sensor node locations, the time and day of the year, both encoded using Eq. (3.1) as for the previous models in order to take into account the cyclic

nature and seasonality of the data. The models were trained using 7,700 pairs of input-output MODIS LST data collected before the year 2018. An amount of 3,300 input-output samples were used for testing.

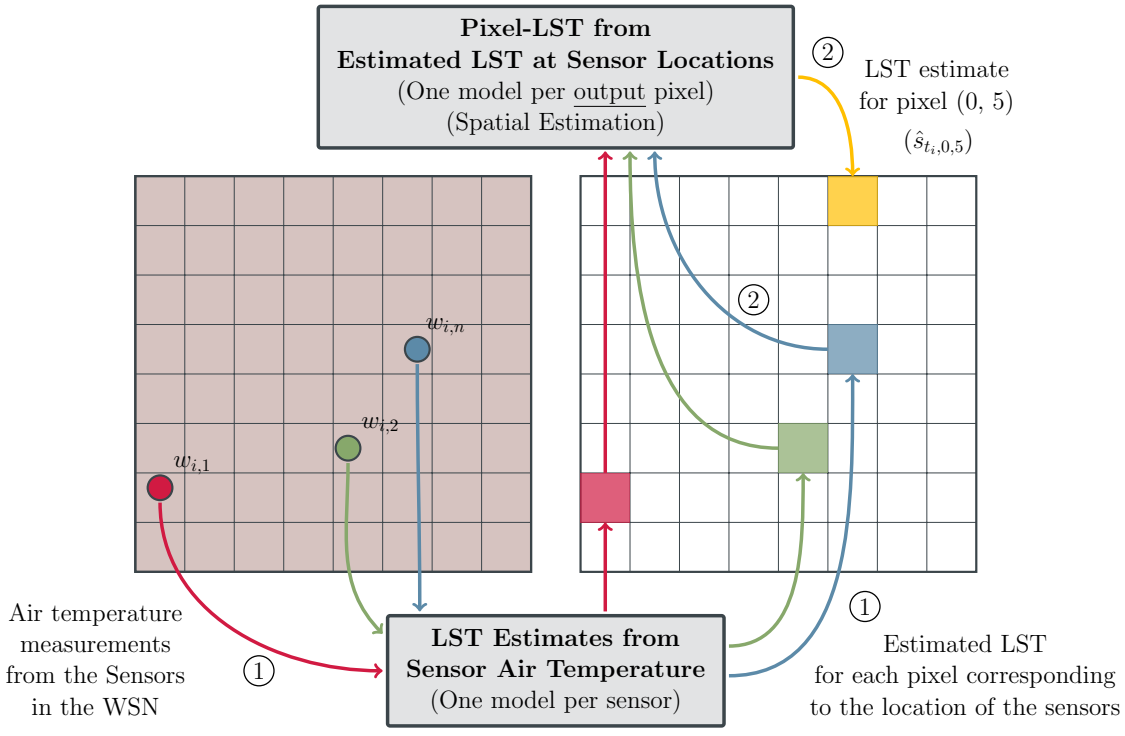

FIGURE 3.12. Spatial LST estimates from LST estimates obtained at the WSN node locations using the WSN air temperature measurements.

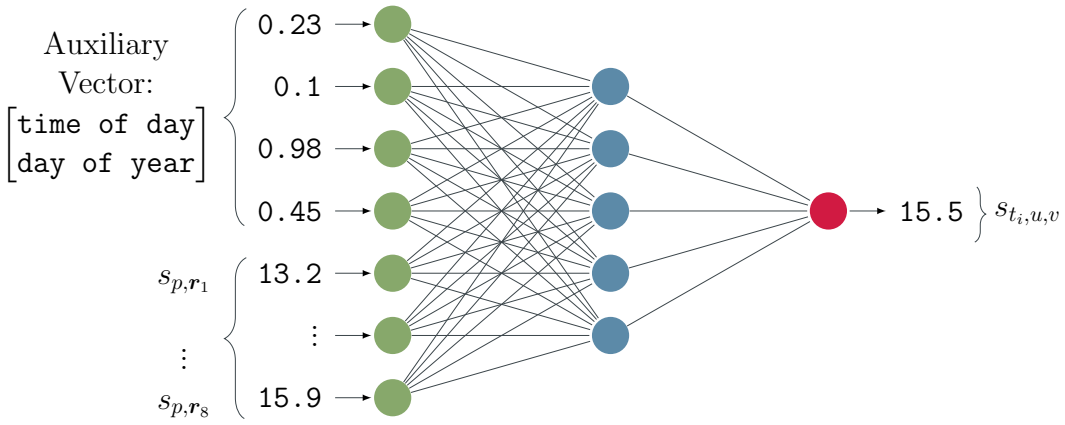

FIGURE 3.13. Graphical representation of the neural network that models the relationship between the LST estimates at a given location, e.g. $(r, c) = (0, 5)$ and the LST estimated at each sensor node. The true sizes of each layer and number of hidden layers are shown in Table 3.8.

TABLE 3.8. Main parameters of the DNN model relating LST estimates at the sensor node locations and LST estimates at other locations.

Optimizer	**Error**	**Activations**	**Layers Size**
ADAM	RMS	ReLU	Input: 12 Hidden: (200, 200, 200) Output: 1

A sequence of 100 samples of the estimated LST and their corresponding ground truth for pixel $(0, 0)$ (upper-left corner) is shown in figure 3.14 to provide a visualization of the accuracy of the estimates. The LST estimation RMSE values for each pixel are shown in figure 3.15a. The RMSE values in figure 3.15a correspond to those obtained with models built using the sensor nodes at their real location. It is possible to notice that the largest errors are concentrated in the lower right area of the image. This is due to the fact that there is another watershed (Maipo Valley) separated by a small dividing range; see figure 2.1a. Hence, the WSN air temperature measurements at the western drainage basin of the Quebrada de Ramón are not very representative of the temperatures in the other basin.

It is possible to simulate the redistribution of the sensors using a sequence of satellite LST measurements and treating the values at certain pixels as ground sensor measurements. Figure 3.15b shows that when eight hypothetical sensors are distributed over a larger area, instead of concentrated in a single region, the RMS error decreases. Hence, future deployments of WSN could implement similar models as the one proposed here to find optimal locations for the sensors. In this study, the sensors of the WSN were concentrated in area due to limits in the communication range because the nodes are solar-powered maintenance-free nodes that are not connected to a standard power distribution grid.

FIGURE 3.14. An example of LST estimates for pixel (0,0) using the LST estimates at the sensor node locations (RMSE: 1.601 °C).

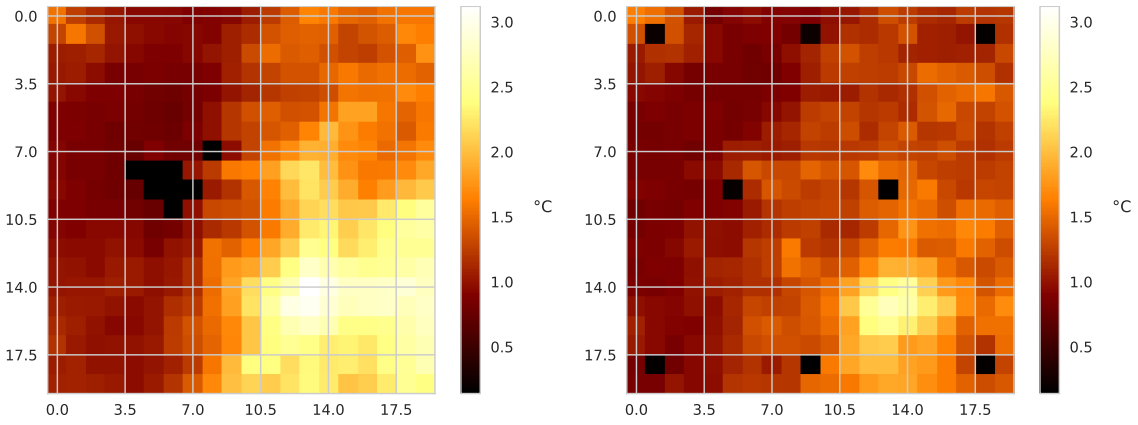

(A) Original
Mean RMSE: 1.488 (SD: 0.639).

(B) Redistribution of Sensors
Mean RMSE: 1.233 (SD: 0.378).

FIGURE 3.15. Land surface temperature RMSE for each pixel model for their respective testing sets.

The LST estimation RMSE is affected not only by the location of the sensors, but also by the number of available sensors. The influence of the number of ground sensors available on the LST estimation RMSE is shown in Figure 3.16a using the sensors at their actual location. The mean RMSE decreases when more sensors are added to the network as expected. The standard deviation practically remains the same independently from the number of sensors added; see Fig. 3.16a. It also was observed in simulations that when more sensors are uniformly added over a larger area, at the points of Fig. 3.15b, the mean LST estimation error decreases faster than when more sensors are added closer to each other within a smaller area; see Fig. 3.16b.

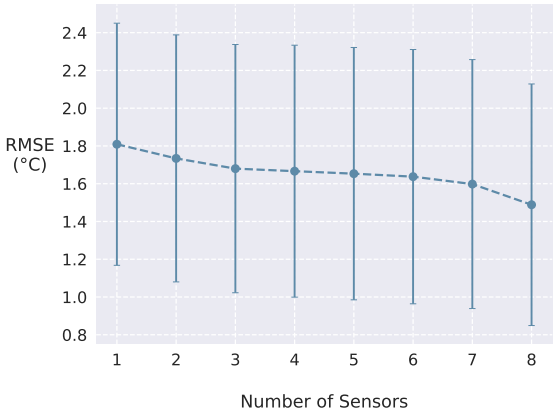

(A) Effect of varying the number of sensors in the original distribution (Fig. 3.15a)

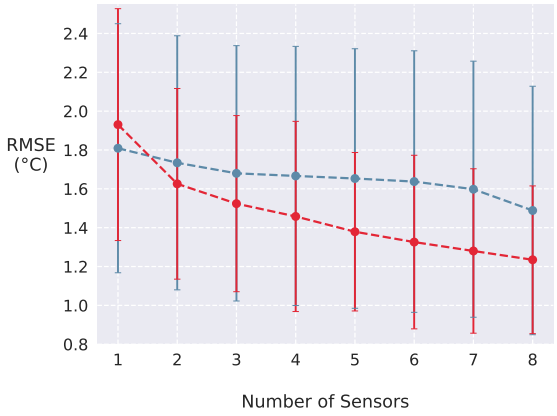

(B) The red line represents the new distribution of sensors (Fig. 3.15b). The blue line is the same graph as the one in Fig. 3.16a, and is displayed for reference.

FIGURE 3.16. Variation of the RMSE when the number of sensors of the WSN is modified.

3.2.5. Spatial Reconstruction of LST Image from LST Measurements at the Sensor Nodes

The proposed approached can be employed to reconstruct LST satellite images with missing data if a set of LST measurements at the location of the sensor nodes is available and treated as outputs of the process that predicts LST measurements from air temperatures measured by the WSN. To this end, the stage that estimates LST from air temperature measurements, which was explained in Section 3.2.3 and illustrated as the lower block in the diagram of Fig. 3.12, is removed. Hence, the LST reconstruction process shown in Fig. 3.17 only employs the spatial LST estimation stage shown in the upper block of Fig. 3.12. It is to be noted that the spatial estimation block could be retrained using satellite LST measurements at other locations different to those of the sensor nodes ir order to implement a reconstruction process that learns the spatial and temporal characteristics of the LST evolution in the area. It also should be noticed that at least one satellite LST measurement is necessary because the imputation process can be employed to estimate the temperatures at the locations of the remaining WSN nodes. However, the reconstructed

LST image will have a larger estimation errors than when there are more LST measurements at the locations of each node available as input to the neural network as discussed in the previous section.

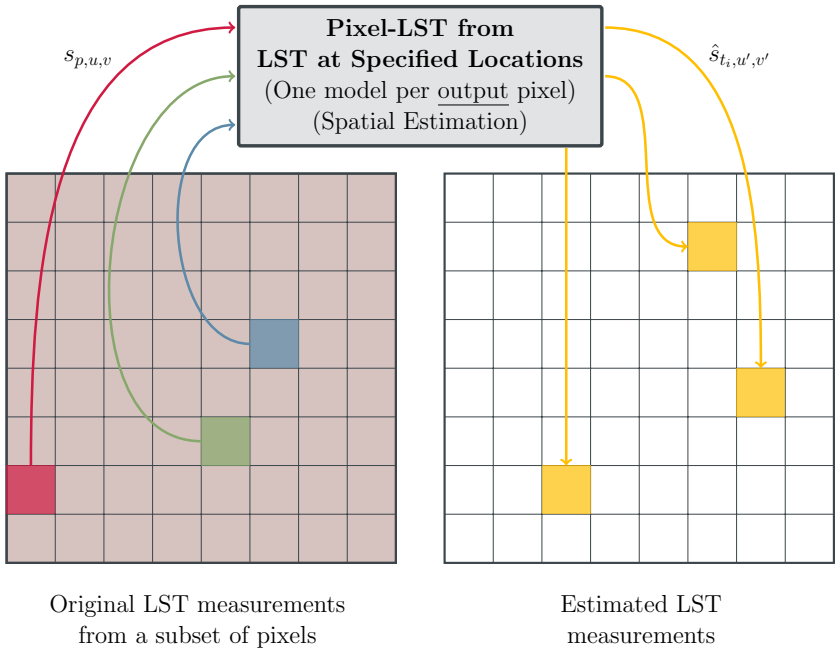

FIGURE 3.17. Spatial LST reconstruction from satellite LST measurements obtained at the locations of at least one of the sensor nodes

.

The proposed LST reconstruction approach provides an alternative to methods that rely on typical spatial interpolation. Standard spatial interpolation procedures often cannot model the topographical and temporal features, thus yielding accuracies that are not suitable for many applications (Zeng et al., 2015). Furthermore, unlike other methods that consider spatio-temporal features in their model to perform the reconstruction, our method does not need other LST images that are near in time to the defective LST image (Zeng et al., 2015; B. Huang et al., 2013).

Chapter 4. RESULTS

The spatio-temporal LST estimation, forecasting and reconstruction results obtained with the proposed WSN and satellite data fusion method are discussed in the next sections. In the computation of the RMSE, the MODIS LST measurements are treated as ground truth. Thus for an estimated LST image $\hat{\boldsymbol{S}}_{t_i,*,*}$, the RMSE with respect to the corresponding p-th satellite LST measurement is given by:

$$RMSE_p = \sqrt{\frac{1}{RC}\sum_{u=1}^{R}\sum_{v=1}^{C}\left(s_{p,u,v} - \hat{s}_{t_i,u,v}\right)^2}, \quad p = 1, 2, \ldots, P.$$

The average RMSE and the RMSE's standard deviation can be computed using the values $RMSE_p$, for the LST satellite images $\boldsymbol{S}_{p,*,*}$, $p = 1, 2, \ldots, P$, in the collection. The following results employed $P = 80$ images acquired during 2018. Each image is $R \times C = 20 \times 20$ pixels.

4.1. LST Spatial Estimation

The averaged RMSE of the estimated LST is 2.21 ± 0.39 °C with confidence level 95%. The standard deviation of the RMSE for the collection of estimated LST images obtained with the proposed approach was 1.8 °C. Considering average span of the diurnal LST variation in the area at the same time of year was 37.4 °C, the mean relative error percentage (RMSE/span) is 5.9%, while the mean relative error percentage of a MODIS LST image would be 1.3% assuming all pixels have a 0.5°C error.

Compared to the best approaches reported in the literature that employ multi-satellite data fusion techniques, such as the STITFM approach by Wu et al. (2015), which uses groups of satellites (Landsat and MODIS) in addition to one geostationary satellite (GOES/SEVIRI) to obtain LST estimates, the proposed approach achieves a similar accuracy levels with additional benefit of providing measurements at twice the frequency of STITFM. Table 4.1 summarizes the performance of the proposed approach compared to that of the STITFM reported in (Wu et al., 2015).

TABLE 4.1. Comparison between the proposed LST estimation approach and the multi-satellite data fusion method for LST estimation proposed by Wu et al. (2015).

Method	**Average Temporal Resolution**	**RMSE (°C)**
Proposed approach	15 min.	2.2
STITFM (Two Satellites)	30 min.	3.3
STITFM (Three Satellites)	30 min.	2.2

An example of the spatial LST estimates obtained with the proposed WSN and satellite data fusion approach is presented in Fig. 4.1, which shows a sequence of *virtual* satellite images generated at a higher temporal rate than that of the MODIS products. The first image in Fig. 4.1 coincides with a MODIS acquisition at time t_0 = 17:25 (UTC-3) on January 3, 2018 (Chilean Summer). Subsequent images, Fig. 4.1 (b) through (g) correspond to the LST estimates very 15 minutes. The sequence shows a peak in land surface temperature at 18:25, 2:31 hours before sunset. The last estimated image, Fig. 4.1 (g) is compared to the ground truth image from MODIS in Fig. 4.1 (h), at time t_0 = 18:55 (UTC-3). The RMSE of the spatial LST estimates is 1.42 °C. The perceived similitude between the estimated image and the ground truth is remarkable.

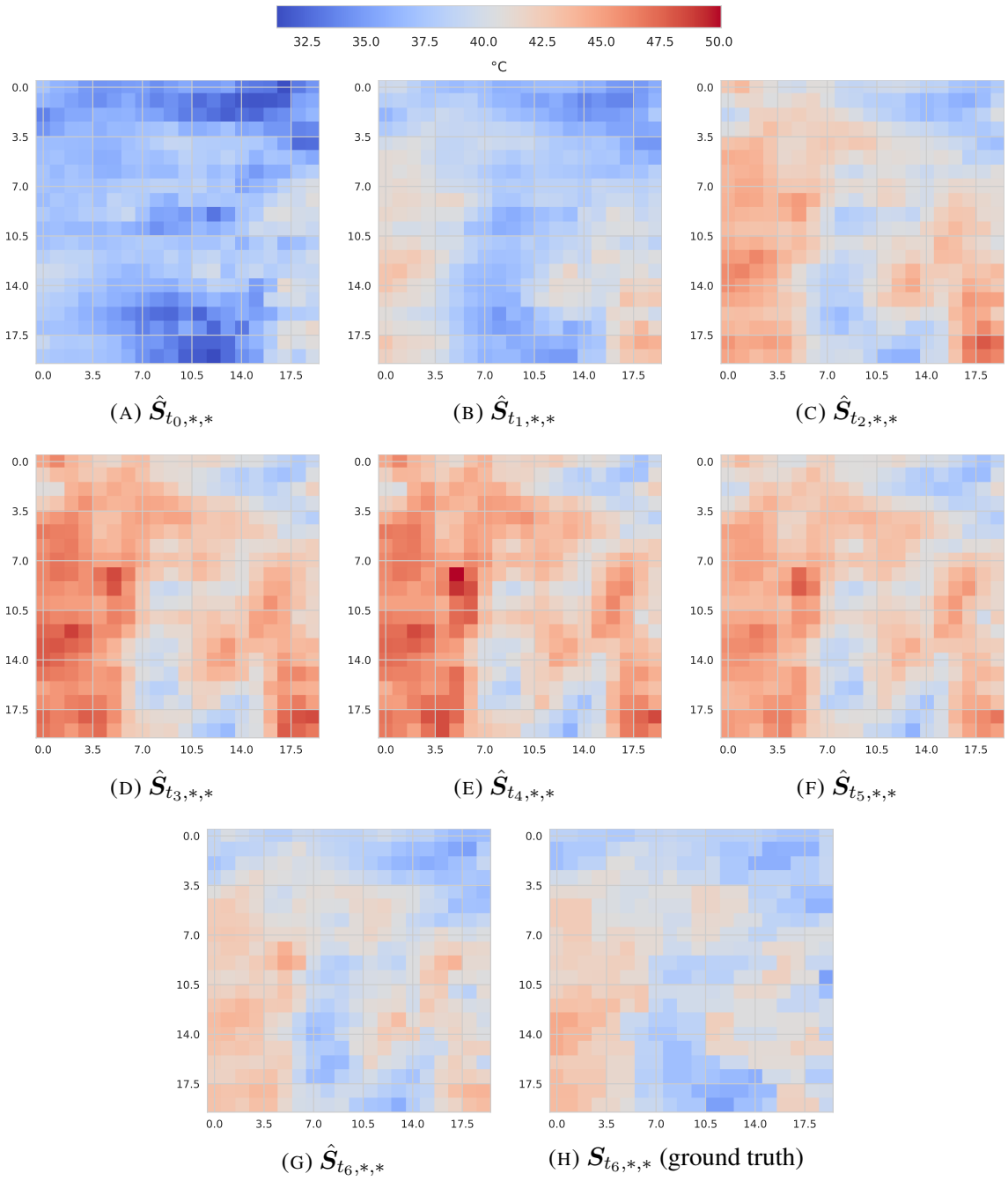

(A) $\hat{\boldsymbol{S}}_{t_0,*,*}$ (B) $\hat{\boldsymbol{S}}_{t_1,*,*}$ (C) $\hat{\boldsymbol{S}}_{t_2,*,*}$

(D) $\hat{\boldsymbol{S}}_{t_3,*,*}$ (E) $\hat{\boldsymbol{S}}_{t_4,*,*}$ (F) $\hat{\boldsymbol{S}}_{t_5,*,*}$

(G) $\hat{\boldsymbol{S}}_{t_6,*,*}$ (H) $\boldsymbol{S}_{t_6,*,*}$ (ground truth)

FIGURE 4.1. Spatial LST estimates every 15 minutes starting at Jan. 3, 2018, 17:25 (UTC-3). The RMS error between the estimation at time t_6 and its corresponding ground truth is 1.212 °C.

4.2. LST Spatial Reconstruction

If the LST measurements obtained from MODIS are used instead of those obtained from the WSN to estimate the LST values in the remaining pixels, for example, to reconstruct a satellite image with missing data except at the locations of the sensor nodes, the average RMSE of the estimated LST image decreases to 1.49 ± 0.14 °C with confidence level 95%. The RMSE's standard deviation for the collection of reconstructed LST satellite images was 0.64 °C. The mean relative error percentage for the reconstruction using the same evaluation scenario is 3.7%.

An example of LST MODIS images with randomly generated missing areas is shown in Figs. 4.2 (a), (d) and (g). The proposed WSN and satellite data fusion approach was employed to spatial LST estimates at the corresponding time instants, shown in Figs. 4.2 (b), (e) and (h). Finally, the missing areas in Figs. 4.2 (a), (d) and (g) are patched with the pixel values of Figs. 4.2 (b), (e) and (h), to obtain the reconstructed images in Figs. 4.2 (c), (f) and (i), respectively.

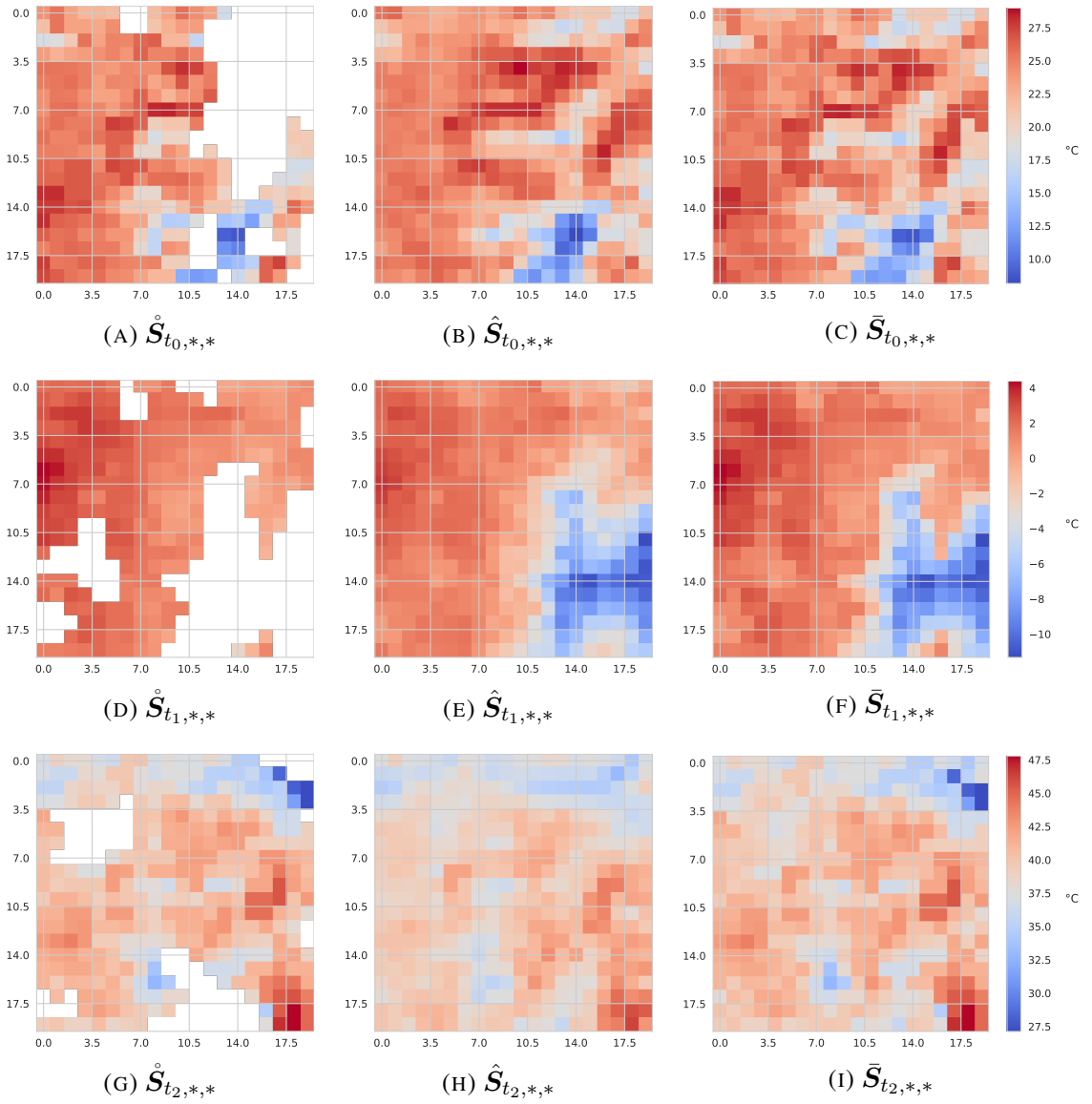

(A) $\mathring{\boldsymbol{S}}_{t_0,*,*}$ (B) $\hat{\boldsymbol{S}}_{t_0,*,*}$ (C) $\bar{\boldsymbol{S}}_{t_0,*,*}$

(D) $\mathring{\boldsymbol{S}}_{t_1,*,*}$ (E) $\hat{\boldsymbol{S}}_{t_1,*,*}$ (F) $\bar{\boldsymbol{S}}_{t_1,*,*}$

(G) $\mathring{\boldsymbol{S}}_{t_2,*,*}$ (H) $\hat{\boldsymbol{S}}_{t_2,*,*}$ (I) $\bar{\boldsymbol{S}}_{t_2,*,*}$

FIGURE 4.2. MODIS LST acquisitions with randomly generated missing areas (a), (d) and (g); estimated LST images (b), (e) and (h); and reconstructed images (c), (f) and (i) at time t_0 = May 10, 2018, 18:30, t_1 = June 1, 2018, 05:50 and t_2 = January 14, 2018, 18:55 (UTC-3).

4.3. LST Spatio-Temporal Forecasting

The proposed WSN and satellite data fusion approach can also be employed for LST spatio-temporal forecasting using the WSN forecasting model presented in Section 3.2.2 to predict future air temperature measurements. The predicted values of future air temperature

measurements are then used to forecasts of future LST images. The evaluation of the spatio-temporal forecasting model with the test data yield a small RMSE of 1.42 °C. Fig. 4.3 shows the predicted LST images computed every 15 minutes, starting at t_0 = March 6, 2018, 04:00 (UTC-3), towards the end of the summer, 3:34 hours before sunrise. The last forecasted image (Fig. 4.3g) is compared to the actual satellite measurement (Fig. 4.3h) at the corresponding time. Once again, a remarkable resemblance between the forecasted LST image and the ground truth can be appreciated.

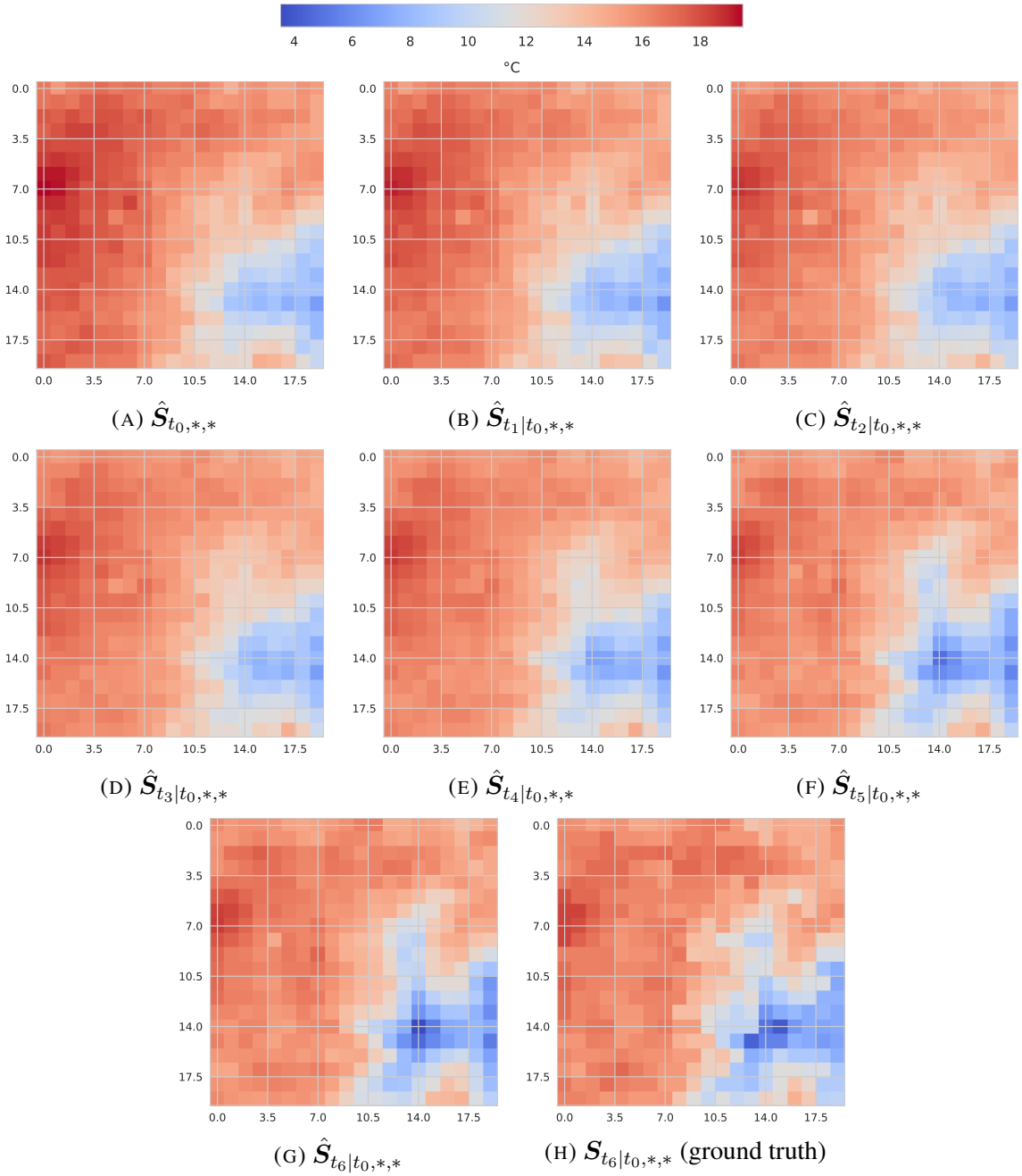

(A) $\hat{\boldsymbol{S}}_{t_0,*,*}$ (B) $\hat{\boldsymbol{S}}_{t_1|t_0,*,*}$ (C) $\hat{\boldsymbol{S}}_{t_2|t_0,*,*}$

(D) $\hat{\boldsymbol{S}}_{t_3|t_0,*,*}$ (E) $\hat{\boldsymbol{S}}_{t_4|t_0,*,*}$ (F) $\hat{\boldsymbol{S}}_{t_5|t_0,*,*}$

(G) $\hat{\boldsymbol{S}}_{t_6|t_0,*,*}$ (H) $\boldsymbol{S}_{t_6|t_0,*,*}$ (ground truth)

FIGURE 4.3. LST spatio-temporal forecasts every 15 minutes starting at t_0 = March 6, 2018, 04:00 (UTC-3). The RMS error between the forecast at time t_6 and its corresponding ground truth is 1.420 °C.

4.4. LST Reprojection Refinement

The transformations that associate remote sensor measurements to a specific map projection involve resampling methods to handle the discrete data. For example, the MODIS Reprojection Tool (MRT) supports three resampling methods: nearest neighbor, bilinear, and cubic convolution. It has been reported that bilinear and cubic convolution methods produce artifacts in the reprojected images and introduce high extrema values. On the other hand, the nearest neighbor algorithm does not introduce artificial values, but can generate significant resolution losses (Neteler, 2010). The proposed approach may be employed to produce smoother LST images taking LST measurements at some image locations as sensor node temperature measurements.

The capability of the proposed approach to generate spatially smoothed LST images that preserve the features of the original measurement and spatio-temporal characteristics learnt by the estimation model are presented in Fig. 4.4, which shows LST images obtained using the nearest neighbor reprojection algorithm in Figs. 4.4 (a), (c) and (e), and the output obtained in Figs. 4.4 (b), (d) and (f) when the proposed LST spatial estimation approach described in Section 3.2.4 is fed with the LST values of the reprojected images in Figs. 4.4 (a), (c) and (e) acquired at time instants t_0 = January 11, 2018, 14:05, t_1 = January 26, 2018, 19:20, and t_2 = February 8, 2018, 05:05. The results show that the proposed WSN and satellite data fusion approach can be used to refine the coarser LST reprojected measurements yielding a smoothed reconstruction that is consistent with the topographical features of the terrain.

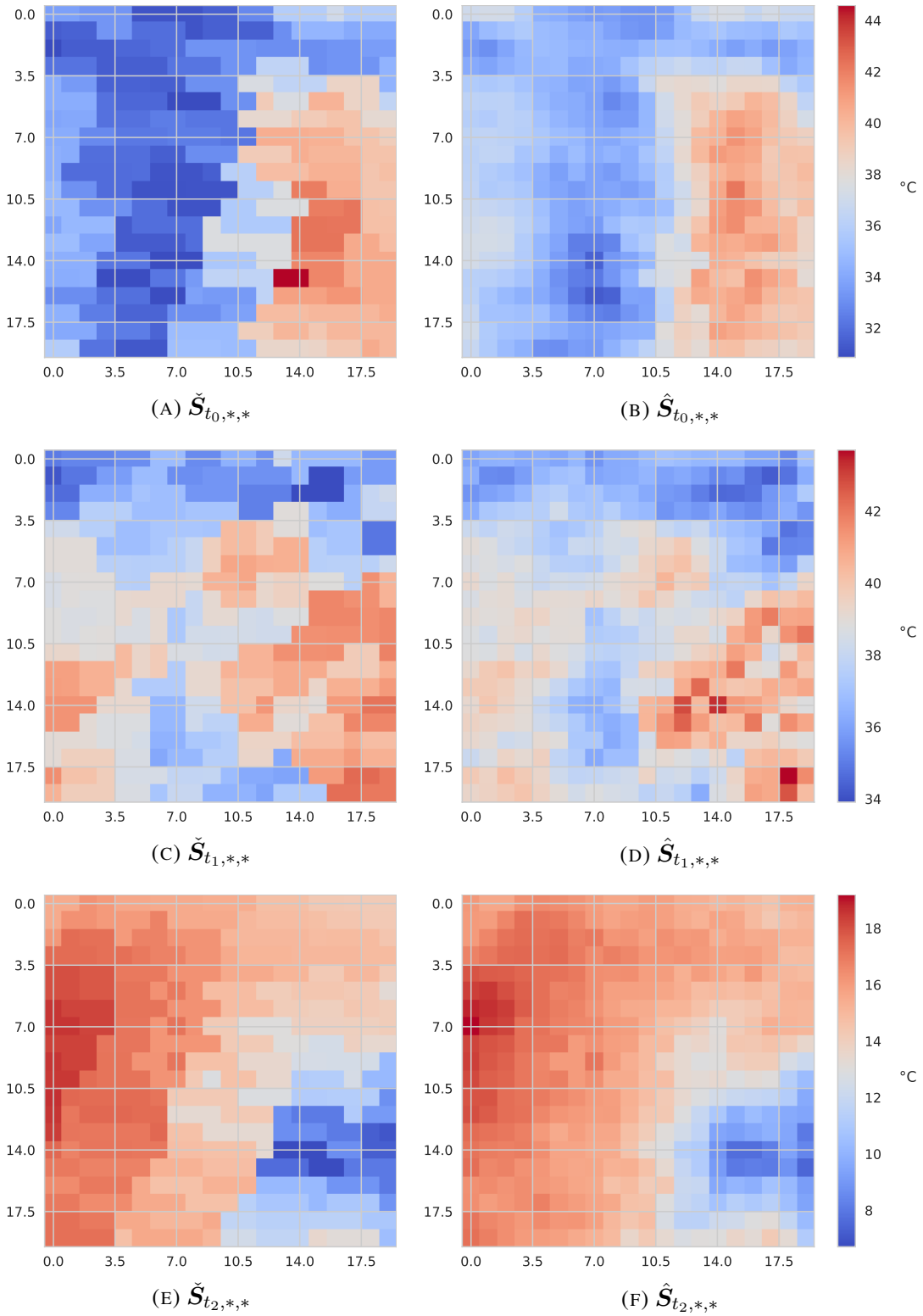

(A) $\check{\boldsymbol{S}}_{t_0,*,*}$ (B) $\hat{\boldsymbol{S}}_{t_0,*,*}$

(C) $\check{\boldsymbol{S}}_{t_1,*,*}$ (D) $\hat{\boldsymbol{S}}_{t_1,*,*}$

(E) $\check{\boldsymbol{S}}_{t_2,*,*}$ (F) $\hat{\boldsymbol{S}}_{t_2,*,*}$

FIGURE 4.4. MODIS LST acquisition with reprojection distortions (a), (c) and (e) and the corresponding refined LST estimated images (b), (d) and (f) at time t_0 = January 11, 2018, 14:05, t_1 = January 26, 2018, 19:20 and t_2 = February 8, 2018, 05:05 (UTC-3).

Chapter 5. CONCLUSION

An approach for wireless sensor network (WSN) and satellite data fusion capable of delivering LST estimates and forecasts at a higher rate than the satellite revisit frequency was presented. To the best of our knowledge, this is the first proposal of a strategy for WSN and satellite data fusion. This allows to combine the higher temporal resolution of the WSN with the higher spatial resolution and larger area coverage of the satellite observations. The approach employs deep neural networks to describe each of the main stages of the LST estimation process, which includes: (i) an imputation model to estimate missing WSN terrestrial air temperature measurements, (ii) a forecasting model for prediction of future WSN air temperature measurements, (iii) a model to estimate LST from air temperature measurements, and (iv) a spatial LST estimation model from LST values computed at the location of the WSN nodes. The last stage can be modified to render the proposed approach useful for spatial reconstruction of LST images that have missing data or to smooth LST image acquisitions that are coarse due to reprojection and resampling artifacts. The RMSE of the spatial LST estimation is on average 2.21 °C on average for an area of 20×20 km with an 8-node WSN deployed in a 5×4 km region located at the Quebrada de Ramón basin east of the city of Santiago, Chile. A similar RMSE was obtained for LST forecasts in a 1.5-hour forecasting horizon. The mean relative error percentage obtained considering the temperature span of the average diurnal LST variation is less than 6%.

The proposed WSN and satellite data fusion strategy can be useful for the applications and is not limited to air temperature and LST measurements. Ongoing research is concerned with the study of the effects of fog and wind measured at the ground level, and model refinements in the presence of cloud cover, in order to improve the accuracy of estimated LST images. Thus the approach may provide a valuable tool for future environmental monitoring and hidrometeorological research.

Bibliography

Aldunate, J., & Oberli, C. (2018). An acquisition scheme for communications in multi-antenna sensor networks with low signal to noise ratio. *International Journal of Sensor Networks*, *27*(4), 259–267.

Benali, A., Carvalho, A., Nunes, J., Carvalhais, N., & Santos, A. (2012). Estimating air surface temperature in Portugal using MODIS LST data. *Remote Sensing of Environment*, *124*, 108–121.

Butenuth, M., Frey, D., Nielsen, A. A., & Skriver, H. (2011). Infrastructure assessment for disaster management using multi-sensor and multi-temporal remote sensing imagery. *International Journal of Remote Sensing*, *32*(23), 8575-8594.

Buyantuyev, A., & Wu, J. (2010). Urban heat islands and landscape heterogeneity: linking spatiotemporal variations in surface temperatures to land-cover and socioeconomic patterns. *Landscape Ecology*, *25*(1), 17–33.

Contreras Vargas, M., Oberli, C., Castro, L., Ledezma Sr, C., Gironas, J., & Escauriaza, C. (2016). A Multidisciplinary Approach for Monitoring Flood and Landslide Hazards: Application to The Quebrada de Ramón Watershed in Central Chile. In *Agu fall meeting abstracts.*

Friedl, M., Schimel, D., Michaelsen, J., Davis, F., & Walker, H. (1994). Estimating grassland biomass and leaf area index using ground and satellite data. *International Journal of Remote Sensing*, *15*(7), 1401–1420.

Goodfellow, I., Bengio, Y., & Courville, A. (2016). *Deep learning*. MIT Press. (`http://www.deeplearningbook.org`)

Hilker, T., Wulder, M. A., Coops, N. C., Linke, J., McDermid, G., Masek, J. G., ... White, J. C. (2009). A new data fusion model for high spatial-and temporal-resolution mapping of forest disturbance based on Landsat and MODIS. *Remote Sensing of Environment*, *113*(8), 1613–1627.

Huang, B., Wang, J., Song, H., Fu, D., & Wong, K. (2013). Generating high spatiotemporal

resolution land surface temperature for urban heat island monitoring. *IEEE Geoscience and Remote Sensing Letters*, *10*(5), 1011–1015.

Huang, R., Zhang, C., Huang, J., Zhu, D., Wang, L., & Liu, J. (2015). Mapping of daily mean air temperature in agricultural regions using daytime and nighttime land surface temperatures derived from TERRA and AQUA MODIS data. *Remote Sensing*, *7*(7), 8728–8756.

Inamdar, A. K., French, A., Hook, S., Vaughan, G., & Luckett, W. (2008). Land surface temperature retrieval at high spatial and temporal resolutions over the southwestern United States. *Journal of Geophysical Research: Atmospheres*, *113*(D7).

Joyce, K. E., Belliss, S. E., Samsonov, S. V., McNeill, S. J., & Glassey, P. J. (2009). A review of the status of satellite remote sensing and image processing techniques for mapping natural hazards and disasters. *Progress in Physical Geography: Earth and Environment*, *33*(2), 183-207.

Junninen, H., Niska, H., Tuppurainen, K., Ruuskanen, J., & Kolehmainen, M. (2004). Methods for imputation of missing values in air quality data sets. *Atmospheric Environment*, *38*(18), 2895–2907.

Ke, L., Ding, X., & Song, C. (2013). Reconstruction of time-series MODIS LST in Central Qinghai-Tibet Plateau using geostatistical approach. *IEEE Geoscience and Remote Sensing Letters*, *10*(6), 1602–1606.

Khan, S. I., Hong, Y., Wang, J., Yilmaz, K. K., Gourley, J. J., Adler, R. F., ... Irwin, D. (2011, Jan). Satellite remote sensing and hydrologic modeling for flood inundation mapping in lake victoria basin: Implications for hydrologic prediction in ungauged basins. *IEEE Transactions on Geoscience and Remote Sensing*, *49*(1), 85-95.

Kloog, I., Nordio, F., Coull, B. A., & Schwartz, J. (2014). Predicting spatiotemporal mean air temperature using MODIS satellite surface temperature measurements across the Northeastern USA. *Remote Sensing of Environment*, *150*, 132–139.

Li, Z.-L., Tang, B.-H., Wu, H., Ren, H., Yan, G., Wan, Z., ... Sobrino, J. A. (2013). Satellite-derived land surface temperature: Current status and perspectives. *Remote Sensing of Environment*, *131*, 14–37.

Lv, B., Hu, Y., Chang, H. H., Russell, A. G., & Bai, Y. (2016). Improving the accuracy of daily PM 2.5 distributions derived from the fusion of ground-level measurements with aerosol optical depth observations, a case study in North China. *Environmental Science & Technology*, *50*(9), 4752–4759.

Martinis, S., Twele, A., Strobl, C., Kersten, J., & Stein, E. (2013). A multi-scale flood monitoring system based on fully automatic MODIS and TerraSAR-X processing chains. *Remote Sensing*, *5*(11), 5598–5619.

Mieslinger, T., Ament, F., Chhatbar, K., & Meyer, R. (2014). A new method for fusion of measured and model-derived solar radiation time-series. *Energy Procedia*, *48*, 1617–1626.

Mutiibwa, D., Strachan, S., & Albright, T. (2015). Land surface temperature and surface air temperature in complex terrain. *IEEE Journal of Selected Topics in Applied Earth Observations and Remote Sensing*, *8*(10), 4762–4774.

Neteler, M. (2010). Estimating daily land surface temperatures in mountainous environments by reconstructed MODIS LST data. *Remote Sensing*, *2*(1), 333–351.

Parastatidis, D., Mitraka, Z., Chrysoulakis, N., & Abrams, M. (2017). Online global land surface temperature estimation from Landsat. *Remote Sensing*, *9*(12), 1208.

Pinto, D., Castro, L., Cruzat, M., Barros, S., Gironás, J., Oberli, C., ... Cipriano, A. (2015). Decision support system for a pilot flash flood early warning system in Central Chile. *International Journal of Social, Behavioral, Educational, Economic, Business and Industrial Engineering*, *9*(3), 990–997.

Quan, J., Zhan, W., Ma, T., Du, Y., Guo, Z., & Qin, B. (2018). An integrated model for generating hourly Landsat-like land surface temperatures over heterogeneous landscapes. *Remote Sensing of Environment*, *206*, 403 - 423.

Shen, H., Huang, L., Zhang, L., Wu, P., & Zeng, C. (2016). Long-term and fine-scale satellite monitoring of the urban heat island effect by the fusion of multi-temporal and multi-sensor remote sensed data: A 26-year case study of the city of Wuhan in China. *Remote Sensing of Environment*, *172*, 109–125.

Sun, D., & Pinker, R. T. (2003). Estimation of land surface temperature from a Geostationary Operational Environmental Satellite (GOES-8). *Journal of Geophysical Research: Atmospheres*, *108*(D11).

Vancutsem, C., Ceccato, P., Dinku, T., & Connor, S. J. (2010). Evaluation of MODIS land surface temperature data to estimate air temperature in different ecosystems over Africa. *Remote Sensing of Environment*, *114*(2), 449–465.

Vidal, A. (1991). Atmospheric and emissivity correction of land surface temperature measured from satellite using ground measurements or satellite data. *Remote Sensing*, *12*(12), 2449–2460.

Wan, Z. (1999a). MODIS land-surface temperature algorithm theoretical basis document (LST ATBD). *Institute for Computational Earth System Science, Santa Barbara*, *75*.

Wan, Z. (1999b, April). *MODIS land-surface temperature algorithm theoretical basis document (lst atbd), ver. 3.3* (Tech. Rep.). Institute for Computational Earth System Science, University of California, Santa Barbara, CA 93106-3060: Institute for Computational Earth System Science, University of California, Santa Barbara.

Wan, Z. (2008). New refinements and validation of the MODIS land-surface temperature/emissivity products. *Remote Sensing of Environment*, *112*(1), 59–74.

Wan, Z. (2014). New refinements and validation of the collection-6 modis land-surface temperature/emissivity product. *Remote Sensing of Environment*, *140*, 36 - 45.

Wu, P., Shen, H., Zhang, L., & Göttsche, F.-M. (2015). Integrated fusion of multi-scale polar-orbiting and geostationary satellite observations for the mapping of high spatial and temporal resolution land surface temperature. *Remote Sensing of Environment*, *156*, 169–181.

Zeng, C., Shen, H., Zhong, M., Zhang, L., & Wu, P. (2015). Reconstructing MODIS LST based on multitemporal classification and robust regression. *IEEE Geoscience and Remote Sensing Letters*, *12*(3), 512–516.

Zhan, W., Chen, Y., Zhou, J., Wang, J., Liu, W., Voogt, J., ... Li, J. (2013). Disaggregation of remotely sensed land surface temperature: Literature survey, taxonomy, issues, and caveats. *Remote Sensing of Environment*, *131*, 119–139.

Zhang, J. (2010). Multi-source remote sensing data fusion: status and trends. *International Journal of Image and Data Fusion*, *1*(1), 5-24.

Zhang, L.-w., Huang, J.-f., Guo, R.-f., Li, X.-x., Sun, W.-b., & Wang, X.-z. (2013). Spatio-temporal reconstruction of air temperature maps and their application to estimate rice growing season heat accumulation using multi-temporal MODIS data. *Journal of Zhejiang University SCIENCE B*, *14*(2), 144–161.